



An Intensity Mapping Detection of Aggregate CO Line Emission at 3 mm

Garrett K. Keating^{1,2}, Daniel P. Marrone³, Geoffrey C. Bower², and Ryan P. Keenan³¹ Harvard-Smithsonian Center for Astrophysics, 60 Garden Street, Cambridge, MA 02138, USA; garrett.keating@cfa.harvard.edu² Academia Sinica Institute of Astronomy and Astrophysics, 645 North A'ohoku Place, Hilo, HI 96720, USA³ Steward Observatory, University of Arizona, 933 North Cherry Avenue, Tucson, AZ 85721, USA

Received 2020 July 2; revised 2020 August 7; accepted 2020 August 17; published 2020 October 1

Abstract

We present a detection of molecular gas emission at $z \sim 1\text{--}5$ using the technique of line intensity mapping. We make use of a pair of 3 mm interferometric data sets, the first from the Atacama Large Millimeter/submillimeter Array (ALMA) Spectroscopic Survey in the Hubble Ultra Deep Field, and the second from a series of Atacama Compact Array (ACA) observations conducted between 2016 and 2018, targeting the COSMOS field. At 100 GHz, we measure nonzero power at 97.8% and 99.9% confidence in the ACA and ALMA data sets, respectively. In the joint result, we reject the zero-power hypothesis at 99.99% confidence, finding $\tilde{I}_s^2(\nu) = 770 \pm 210 \mu\text{K}^2 \text{ Hz sr}$. After accounting for sample variance effects, the estimated spectral shot power is $\tilde{I}_s^2(\nu) = 1010_{-390}^{+550} \mu\text{K}^2 \text{ Hz sr}$. We derive a model for the various line species our measurement is expected to be sensitive to, and estimate the shot power to be $120_{-50}^{+70} \mu\text{K}^2 h^{-3} \text{ Mpc}^3$, $210_{-80}^{+110} \mu\text{K}^2 h^{-3} \text{ Mpc}^3$, and $100_{-40}^{+50} \mu\text{K}^2 h^{-3} \text{ Mpc}^3$ for CO(2–1) at $z = 1.3$, CO(3–2) at $z = 2.5$, and CO(4–3) at $z = 3.6$, respectively. Using line ratios appropriate for high-redshift galaxies, we find these results to be in good agreement with those from the CO Power Spectrum Survey. Adopting $\alpha_{\text{CO}} = 3.6 M_\odot (\text{K km s}^{-1} \text{ pc}^2)^{-1}$, we estimate a cosmic molecular gas density of $\rho_{\text{H}_2}(z) \sim 10^8 M_\odot \text{ Mpc}^{-3}$ between $z = 1\text{--}3$.

Unified Astronomy Thesaurus concepts: Molecular gas (1073); Early universe (435); Star formation (1569); Cosmological evolution (336)

1. Introduction

Tracking the evolution of cold molecular gas over cosmic time has become an active research area in recent years, as the amount of observational data on the molecular gas content of high-redshift galaxies has increased dramatically. Facilities like the Submillimeter Array (SMA; Ho et al. 2004), the Combined Array for Research in Millimeter-wave Astronomy (CARMA; Bock et al. 2006), the Northern Extended Millimeter Array (Guilloteau et al. 1992), the Atacama Large Millimeter/submillimeter Array (ALMA; Wooten 2003), and the Very Large Array (VLA; Heeschen 1975), as well as many others, have increased the number of detections from only a few to thousands over the past two decades (Carilli & Walter 2013; Tacconi et al. 2020). However, most of these measurements are of galaxies that have been optically selected, or are otherwise significantly more luminous than the majority of the star-forming population. Both of these effects may bias the resulting estimates of the high-redshift molecular gas history.

Blind detection of more common galaxies remains an observationally expensive task, with narrow-field surveys only yielding a dozen or so high-fidelity detections of CO in early galaxies (Walter et al. 2014; Pavesi et al. 2018; González-López et al. 2019). Large sky-area surveys capable of performing volume-limited blind surveys at high redshift will likely require significant advancement in instrumentation, with next-generation facilities that are potentially decades away from operation (e.g., Murphy et al. 2017). As a result, there are variations of an order of magnitude in observational constraints and theoretical estimates for the cosmic molecular gas density fueling early star formation at $z \approx 3$ (Obreschkow & Rawlings 2009; Popping et al. 2014, 2017; Sargent et al. 2014; Lagos et al. 2015; Keating et al. 2016; Decarli et al. 2019; Riechers et al. 2019).

A growing number of experiments have sought to use power spectrum methods—like those utilized for measurements of the

cosmic microwave background (CMB; e.g., Kaiser 1982; Meyer et al. 1991; Smoot et al. 1992; Strukov et al. 1992)—for measuring aggregate emission coming from a multitude of galaxies over large volumes. This technique, which is colloquially referred to as “line intensity mapping” (see Kovetz et al. 2017 for a review of the subject), can provide an efficient method for probing faint objects. In line intensity mapping, aggregate emission of galaxies is captured as fluctuations in specific intensity over a three-dimensional volume, where the frequency axis is used as a separate spatial dimension. These fluctuations are characterized by a power spectrum, which measures the variance in intensity as a function of spatial scale. The power spectrum is nominally divided into two regimes: the clustering regime, which is sensitive to large-scale structure, and the shot regime, in which the random distribution of galaxies dominate. Unlike direct detection experiments, where the limiting factor is typically point-source sensitivity, the driving figure of merit for intensity mapping is surface brightness sensitivity, which can be achieved with small aperture telescopes. For the cool-gas tracers of CO and [C II], significant theoretical work has been performed in the past decade (e.g., Righi et al. 2008; Lidz et al. 2011; Visbal et al. 2011; Breyse et al. 2014; Mashian et al. 2015; Padmanabhan 2018; Sun et al. 2019; Yue & Ferrara 2019), and a full range of pathfinder experiments have begun to move forward in earnest (e.g., Pullen et al. 2013; Crites et al. 2014; Uzgil et al. 2014; Bower et al. 2015; Li et al. 2016; Lagache 2018; Pullen et al. 2018).

One such experiment was the CO Power Spectrum Survey (COPSS). COPSS utilized an existing, well-characterized instrument (the Sunyaev–Zel’dovich Array—a subset of CARMA) to provide early constraints on the CO(1–0) power spectrum at 1 cm (27–35 GHz; $z \approx 2.6$). COPSS was divided into two separate stages. The first stage (COPSS I; Keating et al. 2015) made use of an older, previously published data set (Sharp et al. 2010). The second stage (COPSS II; Keating et al. 2016, hereafter

referred to as K16) utilized data from a survey optimized for intensity mapping. The final results of K16 reported a tentative detection of the CO(1–0) power spectrum, having measured the aggregate line emission over a volume of $\sim 10^7 \text{ Mpc}^3$. Shortly thereafter, Yang et al. (2019) reported a similar detection of aggregate line emission from [C II] at $z \approx 2.6$, having extracted the signal in cross-correlation of the Planck 545 GHz intensity map, and Uzgil et al. (2019) placed upper limits on CO line emission utilizing data collected at 3 mm (84–115 GHz) with ALMA. While the results of these three experiments require further observational follow-up, they demonstrate the capabilities of existing instruments and data for placing preliminary intensity mapping constraints.

Following the publication of the COPSS results, we now seek to further explore the potential of intensity mapping experiments to probe high-redshift molecular gas. Within the 3 mm atmospheric window, there are several lines that we expect to be luminous for a Milky Way-like galaxy—e.g., CO(2–1), CO(3–2), and CO(4–3)—which are accessible for $z > 1$ galaxies (Dannerbauer et al. 2009; Daddi et al. 2015). Therefore, intensity mapping analyses targeting this window could offer a relatively low-cost method for detecting molecular gas emission from high-redshift galaxies. The experiment presented here, which we refer to as the Millimeter-wave Intensity Mapping Experiment (mmIME), utilizes a combination of archival and targeted observations. The work presented here is focused on this 3 mm window, with the intention of providing initial constraints on the power spectrum of lines in the millimeter regime, building upon the results of COPSS, probing the shot regime of the power spectrum.

We have structured this paper in the following way. We describe the data used for our analysis in Section 2. We discuss the analysis methods and data verification tests used in processing the data in Section 3, with the results of this analysis found in Section 4. These results are then discussed in further detail in Section 5, with conclusions presented in Section 6. Where appropriate in this paper, we assume a Λ cold dark matter cosmology, with $h = 0.7$, $\Omega_m = 0.27$, $\Omega_\Lambda = 0.73$. Unless otherwise noted, throughout this paper we report uncertainties in terms of the 68.3% confidence interval (i.e., $\pm 1\sigma$).

2. Data

The data used for this analysis originate from two separate projects. A brief summary of the observational data can be found in Table 1. One of these projects is the ALMA Spectroscopic Survey Hubble Ultra Deep Field Large Program (ASPECS LP), described further in Section 2.1. The other project utilized the Atacama Compact Array (ACA; Iguchi et al. 2009), described in further detail in Section 2.2.

2.1. ASPECS Data

A more thorough description of the ASPECS can be found in González-López et al. (2019) and Decarli et al. (2019), though for the sake of completeness, we include a brief description of the project here.

ASPECS is a large-scale program that utilized deep ALMA integrations to measure line and continuum emission from high-redshift galaxies, using data collected at both 3 and 1.3 mm. As we have not utilized the 1.3 mm data in our analyses, we will hereafter only discuss the 3 mm observations, and throughout this paper will refer to the ASPECS LP 3 mm data set as the “ASPECS data.” The 3 mm observations were

Table 1
Summary of Data Sets Used in the Analysis Presented in This Paper

Project Code	Array	Freq. Coverage (GHz)	Effective Sky Area ^a (arcmin ²)	Integration Time (hr)
2016.1.00324.L	12 m	84–115	2.9	38.1
2016.1.01149.S	7 m	94–98, 106–110	9.7	40.2
2018.1.01594.S	7 m	86–94, 98–106	9.8	80.6

Note.

^a Sky area is calculated as $\Omega_B^2 = \int A^2 d\Omega$, where A is the windowing function over the sky area created by the mosaicking pattern of the relevant observations.

conducted during ALMA Cycle 4, in 2016 December. Five separate tunings were used to cover the entirety of Band 3, which spans from 84–115 GHz, with partially overlapping tunings providing added sensitivity between 96 and 104 GHz. The target of these observations was a 4.6 arcmin² region within the Hubble Ultra Deep Field (Beckwith et al. 2006), centered on the position $\alpha = 03^h32^m38.5^s$, $\delta = -27^\circ47'00''$ (J2000). The region in question was covered with a 17-point mosaic, with typical dwell times of 0.5 hr per pointing for each tuning, over the course of ~ 50 tracks total. All data were recorded at 3.906 MHz spectral resolution, with two spectral windows of 1.875 GHz apiece per sideband. Data were collected in the configurations C40-3 and C40-4, with baselines of between 15–460 m and 15–704 m, respectively.

2.2. ACA Data

The ACA, also known as the Morita Array, is a compact interferometer in northern Chile, consisting of twelve 7 m antennas, adjacent to ALMA. It shares much of the same hardware with the larger ALMA array, with the exception of a dedicated FX correlator, with 1.75 GHz of usable bandwidth per spectral window, and two simultaneous spectral windows per sideband recorded during observations. Unlike the larger 12 m array, the ACA remains in a fixed configuration over time, with baselines between 7 and 45 m in length, as shown in Figure 1.

For these observations, we focused on an area of sky within the COSMOS field (Scoville et al. 2007), centered on the position of a source known as AzTEC-3 ($\alpha = 10^h00^m20.7^s$, $\delta = +02^\circ35'17''$, J2000), an ultraluminous infrared galaxy (ULIRG) residing at $z = 5.3$ (Scott et al. 2008; Dwek et al. 2011), which has also been targeted by the VLA and SMA for blind searches for CO emission at high redshift (Pavesi et al. 2018, G. K. Keating et al. 2020, in preparation). A survey area of 15 arcmin² was covered using a 19-point hexagonally packed mosaic, with pointings spaced such that the field was Nyquist sampled at any given frequency within Band 3 (84–115 GHz). Our goal for these observations was to efficiently probe aggregate emission in the 3 mm atmospheric window, using as few tunings as possible and avoiding frequencies with greater atmospheric contributions to the noise (e.g., close to the 118 GHz O₂ line). A total of three tunings were used to cover the spectral window of interest, with data recorded at 7.813 MHz spectral resolution. The first tuning was observed during Cycle 4 (Project ID 2016.1.01149.S) between

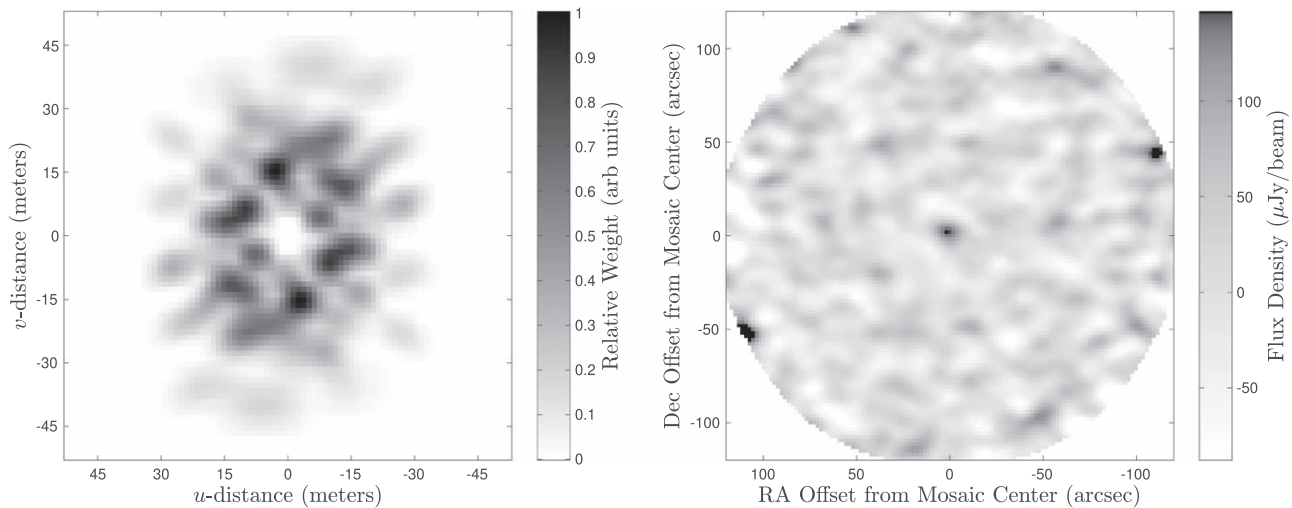


Figure 1. Left: the combined uv coverage of the central mosaic pointing of the COSMOS field, from data collected during the 2016.1.01149.S project (see Table 1 for more details). The uv -plane extent of each visibility weight is determined from the cross-correlation of the illumination patterns of the ACA antennas, which reveals the full range of spatial scales sampled at a uv point. The color scale represents the inverse-variance weight of the data at a given position in the uv -plane, where darker shading indicates greater weighting. Right: the mosaicked continuum image from the entirety of the ACA observations, corrected for primary-beam effects, out to the half-power point of the mosaic pattern. We find a flux density of $150 \pm 30 \mu\text{Jy beam}^{-1}$ at the position of AzTEC-3, in good agreement with previously published results (Riechers et al. 2020).

2016 October 2 and November 10. The latter two tunings were observed during Cycle 6 (Project ID 2018.1.01594.S), between 2018 October 3 and December 11. Dwell times on each pointing of the mosaic were approximately 2 hr per tuning, observed over the course of ~ 60 tracks between Cycle 4 and Cycle 6.

3. Analysis

Analysis of the data closely follows the prescription used for K16. We briefly describe our analysis process, noting in detail where the analysis presented here differs from that of previous works, and direct the reader to K16 and Keating et al. (2015) for further details on the analysis pipeline.

3.1. Data Reduction Pipeline

For all data sets, we utilize the existing ALMA pipeline software (Shinnaga et al. 2015) within the Common Astronomy Software Applications package (CASA; Jaeger 2008) to provide first-order gains and bandpass corrections, flux scaling, as well as noise estimates. The calibrated visibilities and associated metadata are then exported from CASA into our MATLAB⁴-based reduction software package.

After data export, the data from each individual scheduling block are analyzed in their native spectral resolution. An initial round of flagging is performed, which looks for outliers in amplitude when coherently averaging over increasing time intervals for each channel within each baseline. Bandpass solutions are then re-derived and applied to the data set, with typical corrections of order 1% in amplitude, and 1° in phase.

To better characterize the noise properties of the data, we difference visibilities that are adjacent in time (e.g., for a given baseline and spectral channel, the first integration is differenced with the second, and so on), such that the resultant data set is expected to contain only noise. With this noise-only data set, we perform two tasks. First, we fit for antenna-based channel-by-channel system equivalent flux density (SEFD) corrections, which

help account for intermediate frequency or quantization losses that may not be captured by system temperature or efficiency measurements (Keating et al. 2015). Second, we measure the covariance of the noise for all channels within a given spectral window, averaged across all baselines. With the noise properties measured, we average down the data to 15.625 MHz resolution for both ACA and ASPECS data. For both data sets, we find that there are moderate frequency-dependent SEFD corrections required. These corrections are largest at the edges of spectral windows, which may be the result of increased quantization noise in low-amplitude channels, requiring SEFD corrections of order 10%–20% above that estimated by CASA. These corrections appear relatively consistent in data collected within a single ALMA Cycle. The net impact of these corrections can be seen in the agreement between the estimated and measured noise in the image domain, as shown for the ACA data set in Figure 2.

Additional flagging is performed in the spectrally averaged data. The flags are determined from coherent and incoherent sums of data across time intervals from 6 s to ~ 2 hr, evaluated on a per-channel, per-window, and per-baseline basis. This typically discards 3%–5% of data on top of what the CASA pipeline already flags, with the exception of a single track each from the ACA and ASPECS data, where our analysis flagged closer to 20%–30% of data. We discard all data from these two tracks, amounting to a loss of 2% of the total data volume. Bandpass calibration, antenna-based SEFD correction, and noise covariance are re-derived and checked for consistency against that derived for the full resolution data. Antenna gain corrections are then derived and applied to the data, with typical corrections of order 2%–3% in amplitude, and 1° in phase. Where gains are observed to vary by more than 15% between calibration cycles, the offending antenna is flagged. For both the ACA and ASPECS data sets, this is a relatively rare occurrence, affecting less than 0.1% of all data. Generally speaking, we find that both the bandpass and antenna gains shown require only modest corrections after processing through the ALMA pipeline, such that the relative errors on these quantities are expected to be of order less than 1%, and are not expected to be a limiting factor in our analysis. The absolute

⁴ Version 2019a, www.mathworks.com.

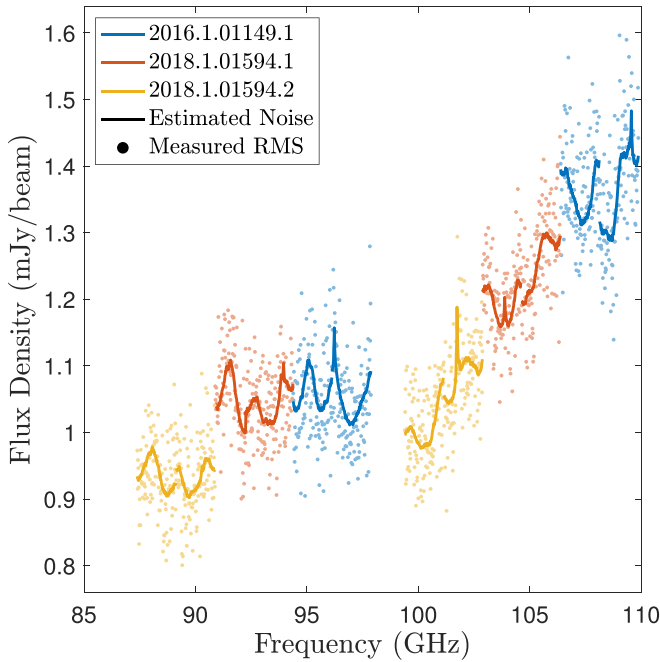


Figure 2. Estimated and measured noise as a function of frequency for the ACA data set. The measured noise is derived from the rms of the inner quarter of mosaicked image, as calculated per 15.625 MHz channel. We find excellent agreement between the predicted and measured values, indicating that the noise properties of the data are well characterized following the application of the SEFD corrections derived by our pipeline. The image noise appears to have a smooth, periodic structure as a function of frequency, the presence of which is not natively captured by the CASA pipeline. Some small peaks in noise can be seen at 96.2, 101.7, and 109.6 GHz, resulting from absorption by stratospheric ozone.

flux uncertainty is estimated to be of order $\sim 5\%$, although we note that this number has been subject to debate within the ALMA community (Bonato et al. 2018). Nevertheless, we expect this uncertainty to be small relative to the overall uncertainty our measurement, barring a high-significance detection ($\gtrsim 10\sigma$).

The data from each scheduling block are then imaged, solely for diagnostic purposes. We show the resulting continuum image from the full set of ACA observations in Figure 1. When imaging the ASPECS data (not shown), we find good agreement with the imaging results published in González-López et al. (2019) for the ASPECS data.

After imaging and inspection, the data are then gridded for power spectrum analysis. Each spectral window in each baseline is separately Fourier transformed along the frequency axis to return to the lag domain and produce what we refer to as “delay visibilities.” The delay visibilities are then gridded into a four-dimensional grid, based on coordinates in (u, v, η, ν_c) , where u and v are the standard interferometer spatial frequency coordinates, measured in units of physical distance (i.e., meters), η is the Fourier dual to the frequency axis (i.e., the lag coordinate), measured in inverse frequency units of ν_c^{-1} , and ν_c is the center frequency of the spectral window that is being gridded. In order to maintain maximum sensitivity, the data are naturally weighted and gridded using a simple, rectangular (i.e., Shah) gridding function, into cells of size 10% of the antenna diameter. This choice of gridding function helps to maximize processing speed, and ensures that the noise within adjacent cells is uncorrelated, at the cost of $\approx 1\%$ – 2% of

our final sensitivity. The sub-pixel mean uv position of the data are also recorded, as well as the estimated noise and windowing functions, the latter of which are determined by the measured channel-to-channel noise covariance.

At the completion of processing for an individual observing block, the gridded data are accumulated across all tracks, and power spectrum analysis is conducted on the aggregate data.

3.2. Power Spectrum Analysis

Throughout this section, we discuss how measurements of the intensity, I , and its Fourier dual, \tilde{I} , are related to the power spectrum measurements that we seek to perform. While previously derived in Keating et al. (2015), our methodology has changed to accommodate the mosaicked data sets used here, versus the single pointings used in COPSS, as has the manner in which we have reported the results (for reasons discussed below). Because of this, we present here our power spectrum methodology in full, noting that both I and \tilde{I} are expressed in brightness temperature units.

The native output of the interferometer is the visibility, \mathcal{V} , representing the Fourier transform of the sky intensity at a given frequency, which can be Fourier transformed across the frequency axis to produce delay visibilities, $\tilde{\mathcal{V}}(u, v, \eta, \nu_c)$, that are functions of angular and frequency wavenumbers (as discussed in Section 3.1), and are directly proportional to \tilde{I} (Bond et al. 1998; White et al. 1999; Morales & Hewitt 2004; Parsons et al. 2012). The immediate goal of our analysis is to measure the variance in intensity over different spatial scales, which by virtue of Parseval’s theorem, is equivalent to measuring the power, \tilde{I}^2 , over a set of Fourier modes, where

$$\begin{aligned} \tilde{I}^2(u, v, \eta, \nu_c) \\ = \frac{\tilde{\mathcal{V}}^*(u, v, \eta, \nu_c) \cdot \tilde{\mathcal{V}}(u, v, \eta, \nu_c)}{\iiint W(l, m, \nu) \cdot W(l, m, \nu) dl dm d\nu}. \end{aligned} \quad (1)$$

In Equation (1), the term in the denominator serves as a normalization factor, where $W(l, m, \nu)$ is the windowing function of the measurement in question. For a measurement that is uniformly weighted across both the plane of the sky and the spectral axis, the denominator simplifies to $B_{\text{surv}}\Omega_{\text{surv}}$, where B_{surv} is the bandwidth of the observation and Ω_{surv} is the sky area of the survey.

The typical data product of intensity mapping analysis is the power spectrum, $P(k, z)$, or its dimensionless counterpart, $\Delta^2(k, z)$. Both are expressed as functions of wavenumber, k , and redshift, z , and can be further defined as

$$\begin{aligned} \Delta^2(k, z) &\equiv \frac{k^3}{2\pi^2} P(k, z), \\ &= \frac{k^3}{2\pi^2} X^2 Y \langle \tilde{I}^2(u, v, \eta, \nu_c) \rangle_{T(u, v, \eta, z, \nu_c)=k}. \end{aligned} \quad (2)$$

In Equation (2), T is a coordinate mapping function between wavenumber units, from the observed (u, v, η, ν_c) to the comoving spatial wavenumber, k , at a given redshift, z , where

$$T(u, v, \eta, z, \nu_c) = 2\pi \left(\frac{u^2 + v^2}{X^2(z)} + \frac{\eta^2}{Y^2(z, \nu_c)} \right)^{1/2}. \quad (3)$$

In Equations (2) and (3), the values of X and Y are used for unit conversion between observed and physical units

(Parsons et al. 2012), which can be expressed as

$$X(z) = D_M(z), \quad (4)$$

$$Y(z, \nu_r) = \frac{c(1+z)^2}{H_0 E(z) \nu_r}. \quad (5)$$

In Equation (4), D_M refers to the comoving radial distance. In Equation (5), c is the speed of light, H_0 is the Hubble constant at $z = 0$, $E(z)$ is the dimensionless Hubble parameter, and ν_r is the rest frequency of the spectral line under consideration.

There is an intrinsic assumption in Equation (2), in that it effectively requires one to choose a singular redshift (or spectral line) to be the source of the line emission being measured. At 3 mm, we expect multiple lines to have contributions to \tilde{I}^2 , without a simple way to separate individual power spectrum components of each line. In the presence of large-scale structure, one can use the relative anisotropies in the 3D power spectrum to separate out their contributions (Cheng et al. 2016). However, over the wavenumbers considered here, we expect the measurement to be solely sensitive to the small-scale fluctuations driven by individual galaxies, typically referred to as the shot power (Gong et al. 2011; Lidz et al. 2011), $P_{\text{shot}}(z)$. Barring cross-correlation or exhaustive imaging efforts, we risk making an arbitrary choice.

To sidestep this problem, we consider what we refer to as the “spectral shot power,” $\tilde{I}_s^2(\nu)$, which can be calculated by summing \tilde{I}^2 over all wavenumbers with u , v , and η greater than some minimum value, set by the scales at which we expect the contributions of large-scale structure to be minimal ($k \gtrsim 1 \text{ Mpc}^{-1}$). It describes the minimum variance in intensity (absent resolving out individual galaxies) one expects in a power spectrum measurement, varying only as a function of frequency.

To measure $\tilde{I}_s^2(\nu)$, we must first calculate \tilde{I}^2 , which we do with the the following estimator:

$$\tilde{I}^2(u, v, \eta, \nu_c) = \frac{\sum_i \sum_j [\psi_{ij} \tilde{V}_i^* \phi_{ij} \tilde{V}_j w_{ij}] - \mathcal{A}_i}{\sum_i \sum_j [w_{ij}] - w_{\mathcal{A}_i}}. \quad (6)$$

In Equation (6), we are effectively taking a weighted sum of the set of all delay visibilities cross-multiplied against one another, to produce an estimate of \tilde{I}^2 as a function of u , v , η , and ν_c . ϕ is a phase rotation term required when cross-multiplying delay visibilities with different phase centers—i.e., data from different mosaic pointings. ψ is a normalization term that accounts for the combined the windowing functions of the i th and j th delay visibilities, which can be further defined as

$$\psi_{ij} = \left[\iiint (A_i^* B_i) \cdot (A_j^* B_j) dl dm d\nu \right]^{-1}, \quad (7)$$

where A and B are the windowing function in the plane of the sky and across the frequency axis, respectively. For our analysis, we take $B(\nu) = 1$ over the frequency window of the measurement (and zero outside of this window), and A is set by the primary-beam pattern of the antenna, centered on the mosaic pointing for the given delay visibility. The correlated product of a given pair of modes is weighted by the function w_{ij} , which can be further defined as

$$w_{ij} = \frac{C_{ij}}{\sigma_i^2 \sigma_j^2}, \quad (8)$$

where C_{ij} is the expected signal covariance between modes, and σ_i^2 is the estimated noise variance.

After normalization and weighting, the \mathcal{A}_i term in Equation (6) is needed to debias the estimator. This factor is the weighted autocorrelation of all delay visibilities within a single gridded cell, which removes this bias assuming that the noise in adjacent cells is uncorrelated. We similarly subtract off the sum of all weights for the autocorrelations, $w_{\mathcal{A}_i}$, in order to properly normalize \tilde{I}^2 .

With our measurements of \tilde{I}^2 in hand, we are now able to calculate quantity \tilde{I}_s^2 by averaging over the available ensemble of modes,

$$\tilde{I}_s^2(\nu) = \frac{\sum_{u,v,\eta} \tilde{I}^2(u, v, \eta, \nu_c) \sigma_{\tilde{I}^2}^{-2}(u, v, \eta, \nu_c)}{\sum_{u,v,\eta} \sigma_{\tilde{I}^2}^{-2}(u, v, \eta, \nu_c)} \quad (9)$$

where $\sigma_{\tilde{I}^2}$ is the estimated noise variance of \tilde{I}^2 .

Though division of its power into specific lines requires a model or some other constraint, the spectral shot power represents the following summation:

$$\tilde{I}_s^2(\nu) = \sum_{\text{all lines}} \frac{P_{\text{shot,line}}(z)}{X(z)^2 Y(z, \nu_{r,\text{line}})}, \quad (10)$$

where $P_{\text{shot,line}}(z)$ is the shot power for a given spectral line at a given redshift, z , which is set by the rest frequency of the line in question, $\nu_{r,\text{line}}$, and the frequency at which the spectral shot power is being evaluated. The primary advantage of using $\tilde{I}_s^2(\nu)$ is that it requires no assumptions about the underlying cosmology, nor division of the signal into separate redshift bins—it is solely based in observable units, which we typically express as $\mu\text{K}^2 \text{ Hz sr}$. We therefore find it appropriate for the measurements presented here, and will express our results in units of $\tilde{I}_s^2(\nu)$, unless otherwise noted.

To verify that our analysis methodology is correct, we run a series of validation tests that simulate a mosaicked observation with both the ACA and ALMA 12 m arrays at 100 GHz in the presence of a blank sky, and then again with in the presence of a background population of line emitters with known number density. For both, we run a series of 10^4 trials separately for simulated versions of the 7 and 12 m arrays to verify that our noise estimates and power spectrum estimator are correct. In both cases, we find good agreement for both to within $\sim 1\%$ of expectations, in line with what one would expect given the number of trials run.

In our analysis, we exclude a subset of modes from our measurement that have the potential to resolve out the emission from individual galaxies. We exclude baselines of length $\gtrsim 100 \text{ k}\lambda$, to avoid resolving sources that are $\lesssim 2''$ in diameter, which is expected to cover the population of interest (Tacconi et al. 2013). We similarly exclude modes where $\eta \gtrsim 500$ to avoid resolving sources an FWHM line width of $\lesssim 300 \text{ km s}^{-1}$. We discuss in further detail the impact this choice of threshold for η in Appendix A.

3.2.1. Impact of Continuum Foregrounds

Compared to the sky at 30 GHz (i.e., the frequency at which COPSS was observed), the continuum foregrounds—particularly those arising from individual point sources—are relatively weak. At the angular scales considered in this measurement ($\theta < 1'$), for targets well outside of the plane of the Galaxy

Table 2
Spectral Shot Power and Jackknife Measurements

Jackknife Test	ASPECS Data		ACA Data		Joint Result ^a	
	Result	PTE	Result	PTE	Result	PTE
Couplet	-330 ± 250	0.18	310 ± 660	0.64	-250 ± 230	0.28
First-last	610 ± 390	0.12	-310 ± 520	0.55	280 ± 310	0.38
Even-odd	400 ± 380	0.29	330 ± 540	0.54	380 ± 310	0.22
Cross-win	300 ± 240	0.21	760 ± 440	0.09	410 ± 210	0.05
Diff-pol	190 ± 240	0.44	440 ± 440	0.32	250 ± 210	0.25
High- η	-20 ± 100	0.86	170 ± 190	0.37	20 ± 80	0.78
Science result	730 ± 240	<0.01	890 ± 440	0.02	770 ± 210	<0.01

Notes. All values are in units of $\mu\text{K}^2 \text{ Hz sr}$.

^a Results calculated using an inverse-variance-weighted sum of both data sets.

(such as those studied here), the primary continuum contaminant at 3 mm is expected to arise from the contributions of individual point sources (Reichardt et al. 2012; Planck Collaboration et al. 2015). While these contributions are generally weak, in aggregate they can contribute more power than the line emission of interest.

Rather than attempting to subtract out individual sources, which may introduce its own set of artifacts and systematics, we seek a different method to eliminate the power from these potential contaminants. As these continuum sources are expected to be spectrally smooth, their contributions will primarily contaminate modes where $\eta \sim 0$. As Keating et al. (2015) demonstrated, discarding the plane of modes at $\eta = 0$ can dramatically reduce the power from continuum sources, even in the presence of moderate gain errors, at the cost of some sensitivity in our power spectrum analysis.

Adopting the 3 mm source count model of Zavala et al. (2018), we find that by removing the $\eta = 0$ modes reduces the contaminant power to $\lesssim 0.1 \mu\text{K}^2 \text{ Hz sr}$. We note that without excluding these modes, the mean contaminant power rises to $\sim 200 \mu\text{K}^2 \text{ Hz sr}$ for both the ASPECS and ACA data sets, which is potentially comparable to the power arising from line emission. Even screening out point sources above the imaging threshold of ASPECS ($\sim 30 \mu\text{Jy}$), there still exists power of order $\sim 50 \mu\text{K}^2 \text{ Hz sr}$. As this is comparable to our estimated error from thermal noise alone, we choose to exclude the $\eta = 0$ modes, at the cost of 3% of the final sensitivity of our power spectrum measurement.

3.2.2. Jackknife Analysis

To verify that our power spectrum measurement is free of significant systematics that may otherwise corrupt our result, we perform a series of jackknife analyses, where the data are combined in such a way that the astrophysical signal in question is subtracted or otherwise made incoherent. We expect the resulting power spectra to be consistent with a null result, so detections of nonzero power are indicative of contaminating signals that are unrelated to the line emission we seek to measure.

We perform six jackknife tests with our data. The following four were previously used in the COPSS survey. The “couplet” test difference visibilities that are adjacent in time, subtracting data from one integration from the integration immediately following it. The “first-last” test differences the sum of all data taken during the first half of all scheduling blocks from the sum of all data taken during the second half. Similarly, the

“even-odd” test differences the the sum of all data taken during even-numbered observing blocks and the sum of all odd-numbered observing blocks. Finally, the “cross-win” test correlates modes in different redshift windows, but the same position in (u, v, η) , where the spectral lines of interest are not expected to be correlated between different volumes for the modes that we measure (though the same may not be true of continuum contaminants or systematics).

In addition to the previously used jackknife tests, we include two new tests in the analysis presented here. The first test is one we refer to as “diff-pol,” which leverages the dual-polarization capabilities of ALMA. As the CO signal itself is expected to be unpolarized, we expect that differencing the vertical and horizontal polarization visibilities from one another will remove the signal of interest, but potentially leave behind systematics that are seen preferentially in one polarization over another. The second test is referred to as “high- η ,” where only modes with $\eta > 500$ are included, under the expectation that they resolve out the bulk of the individual sources in frequency space, leaving little to no power from astronomical sources (discussed in Appendix A.1).

The results from our jackknife analysis are shown in Table 2 and in Figure 3. For both the ASPECS LP and ACA data sets, we find that the results are generally consistent with that which we would expect from noise. Within the results of the ASPECS data, we do find a small excess of power for the first-last jackknife test at $k_{\text{CO}(3-2)} \approx 50 h \text{ Mpc}^{-1}$, spread over several separate bins, none of which exceed 2σ in significance. Optimally weighting over the range of $k_{\text{CO}(3-2)} = 40\text{--}90 h \text{ Mpc}^{-1}$, we measure power at 2.9σ , with the likelihood of a noise-like event to produce equal or greater power (probability to exceed; PTE) equal to approximately 1 in 300. Although not inconsistent with a noise-like event, given the ~ 200 individual measurements in Figure 3, we have explored this result in greater detail. We find no particular redshift or track that dominates the signal. This jackknife is the least sensitive of the six, in part because the slow changes in the configuration of ALMA 12 m array over the course of the observations cause the uv coverage of the first and last halves of the data to be somewhat disjoint, which leaves few measurements per uv cell for differencing. In such cases, the noise distribution becomes skewed (K16), making the likelihood of positive outlier events higher than expected relative to a normal distribution. Evaluating across all wavenumber bins, we find a reduced chi-squared value of $\chi_{\text{red}}^2 = 1.04$ (with 18 degrees of freedom), consistent with noise. As our final results are reported as band-averaged values, and as the band-averaged jackknife results for both data sets show less

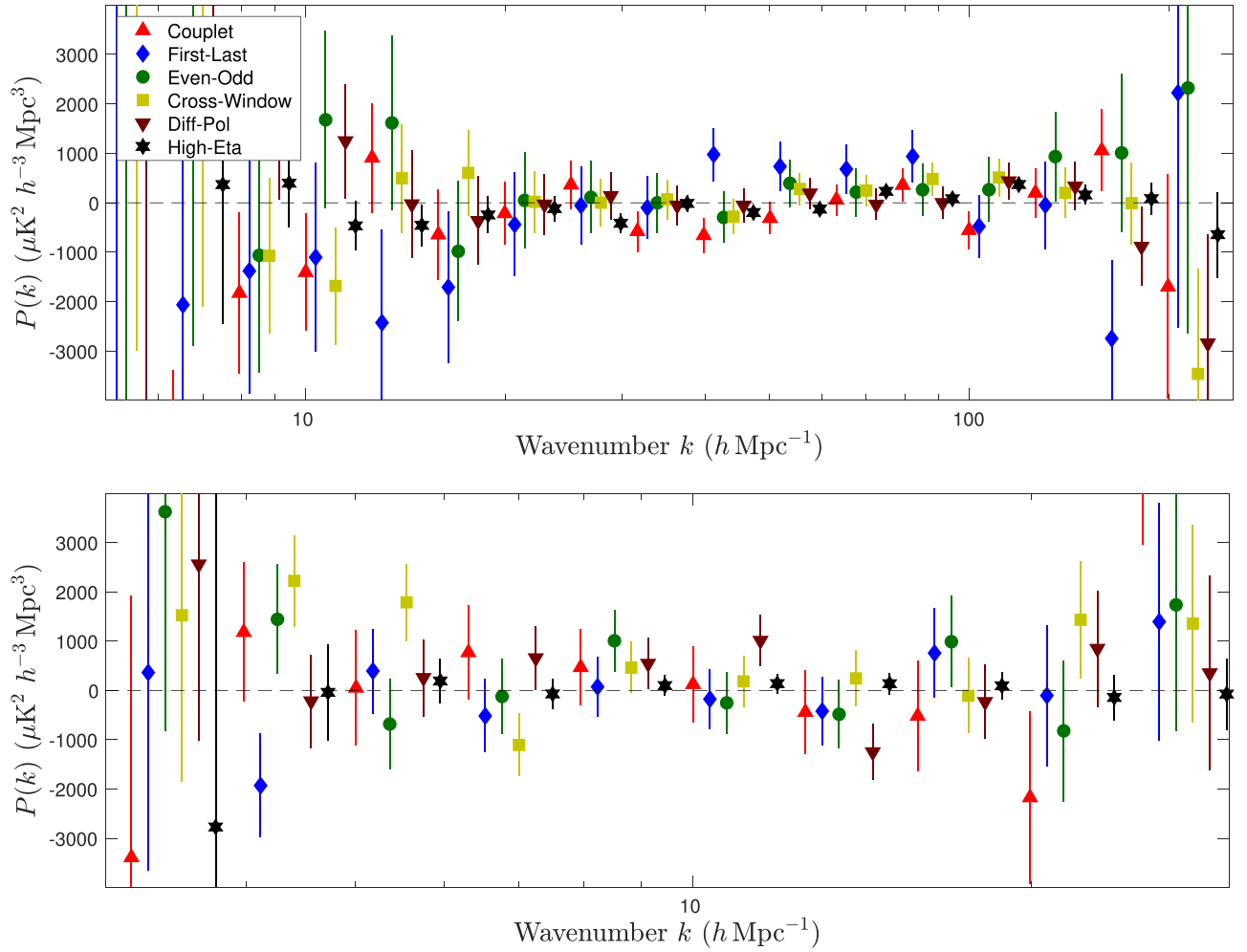


Figure 3. Power measured in our jackknife analyses as a function of wavenumber k , projected to the CO(3–2) frame, in units of $\mu\text{K}^2 h^{-3} \text{Mpc}^3$, for the ASPECS (top panel) and ACA (bottom panel) data sets. The results of the analyses of both data sets are consistent with noise, with the largest outliers observed at 2.4σ for both the ASPECS and ACA results. Both are consistent with what one would expect for a noise-like distribution, given the number of data points produced in our analysis.

than 2σ significance, we conclude that the data are sufficiently free of systematics for power spectrum analysis.

As in K16, we perform one additional jackknife-like test, where the phases of the individual cells in each gridded data set are randomized before accumulation and correlation, in order to further validate our estimated uncertainties. We find that the noise estimates from this test agree with those derived from thermal estimates to within the nominal sample variance once expects from 100 trials (i.e., 10% uncertainty).

4. Results

Power spectrum results are shown in Figures 4 and 5, and are reported alongside those from the jackknife analysis in Table 2.

We measure $\tilde{I}_s^2(\nu) = 730 \pm 240 \mu\text{K}^2 \text{Hz sr}$ for the ASPECS data. Projecting to the reference frame appropriate for CO(3–2), we find $P_{\text{CO}(3-2)} = 370 \pm 120 \mu\text{K}^2 h^{-3} \text{Mpc}^3$, with the greatest sensitivity between $k = 20$ and $100 h \text{Mpc}^{-1}$. Over this range, we expect the measurement to be completely dominated by shot power, with negligible contributions from large-scale structure.

For the ACA data, we measure $\tilde{I}_s^2(\nu) = 890 \pm 440 \mu\text{K}^2 \text{Hz sr}$. Projecting our results for to that for CO(3–2), we find $P_{\text{CO}(3-2)} = 460 \pm 230 \mu\text{K}^2 h^{-3} \text{Mpc}^3$, with the greatest sensitivity between $k = 4$ and $20 h \text{Mpc}^{-1}$. Similar to the results

from ASPECS, we expect this measurement to have negligible contributions from large-scale structure.

Combining both data sets and weighting by the inverse instrument noise variance, we find $\tilde{I}_s^2(\nu) = 770 \pm 210 \mu\text{K}^2 \text{Hz sr}$. With this result, we are able to reject the zero-power hypothesis ($\tilde{I}_s^2(\nu) = 0$) to 99.99% confidence, signifying that the measured power is unlikely to arise from noise-like fluctuations in the data alone.

4.1. Impact of Source Line Widths

For large values of η , we expect to resolve the lines of individual galaxies, which will suppress the power measured. Our choice to exclude modes where $\eta > 500$ was made in part to allow for a consistent comparison between the results presented here and those from K16. However, as discussed in Appendix A, this choice will at least partially resolve galaxies with line widths of $\gtrsim 300 \text{ km s}^{-1}$. As such objects have been previously observed at high redshift (e.g., Tacconi et al. 2013; Walter et al. 2014; González-López et al. 2019), we verify here our assumption that such effects are not affecting our measurements.

A detailed accounting of this effect—and an estimate for a potential correction factor to our measurement—would require modeling that is well beyond the scope of the work presented

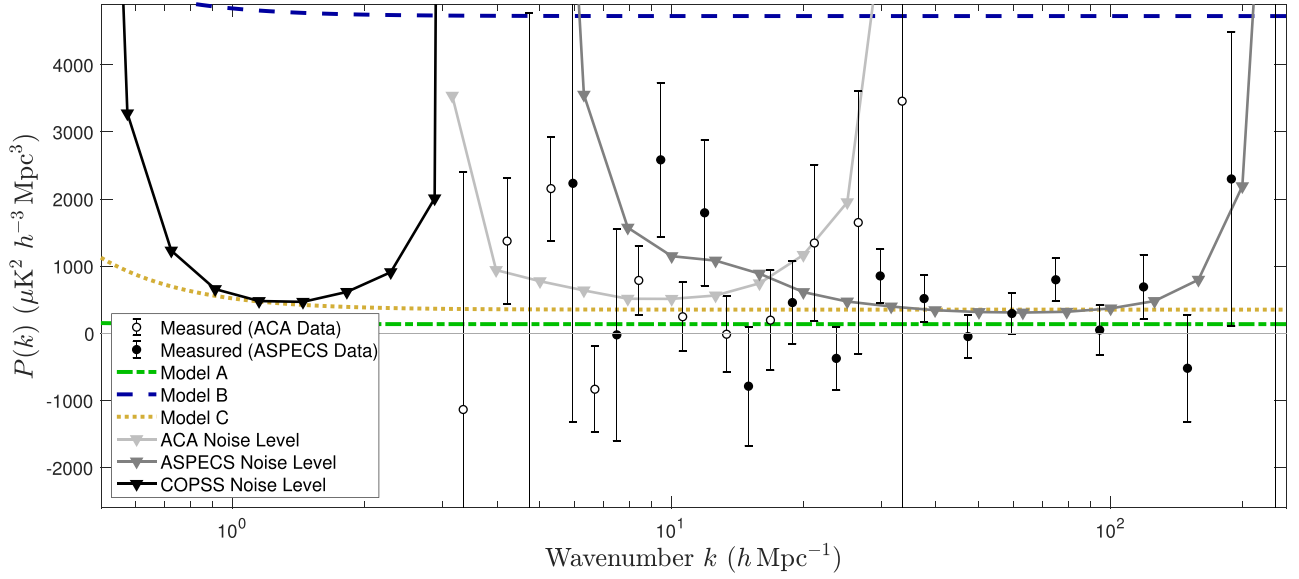


Figure 4. Power measured in our primary analysis of the two data sets discussed in Section 2, in units of $\mu\text{K}^2 h^{-3} \text{Mpc}^3$, measured as a function of wavenumber k , and projected for the CO(3–2) line at redshift $z \approx 2.5$. Shown separately are the results of our power spectrum analysis of the data from ACA (open circles) and ASPECS (filled circles) data, with the results logarithmically binned over intervals of 0.1 dex. The relative 1σ uncertainties for each wavenumber bin are also shown for ACA (light gray triangles) and ASPECS (dark gray triangles). For comparison, the 1σ uncertainties from COPSS are also shown (black triangles), normalized by Equation (14) for CO(3–2), using $r_{3,1} = 0.42$ (Daddi et al. 2015). Also shown for comparison are Model A and Model B of Pullen et al. 2013, which have been similarly normalized to CO(3–2). Model C has been generated using the results of Section 5.3, setting $\langle T_b \rangle^2 b^2 = 100 \mu\text{K}^2$ and $P_{\text{shot}} = 2000 \mu\text{K}^2 h^{-3} \text{Mpc}^3$ for CO(1–0), and is included for illustrative purposes only.

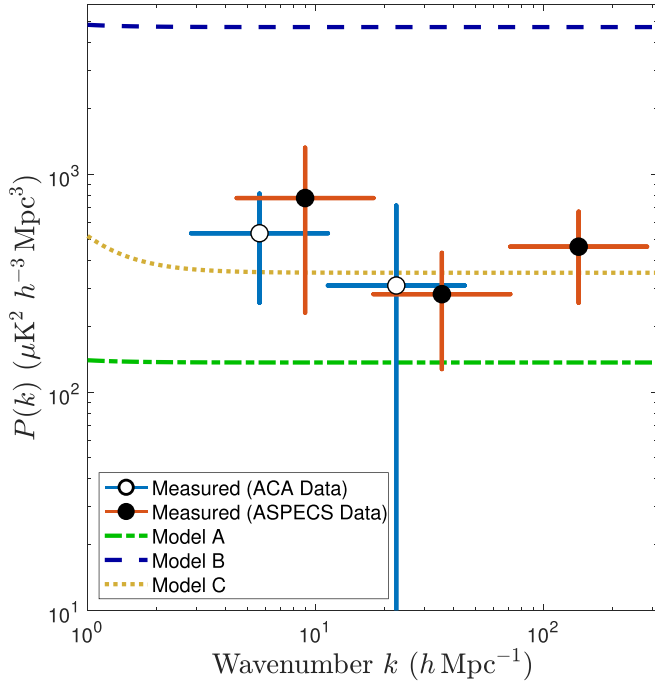


Figure 5. Power measured as a function of wavenumber k , projected for the CO(3–2) line at redshift $z \approx 2.5$. The points have been binned on a logarithmic interval of 0.6 dex (compared to the 0.1 dex binning used in Figure 4).

here. However, a simpler validation test is to evaluate our results considering a smaller range for the allowed values of η . Therefore, we recalculate our results using only those modes where $\eta < 250$, which ought to substantially reduce these source-resolving effects for galaxies with line widths of $\gtrsim 300 \text{ km s}^{-1}$. If galaxies of line width $\sim 600 \text{ km s}^{-1}$ (the maximum line width found for a galaxy in the ASPECS data (González-López et al. (2019))) dominate our

measurement, then we expect the power measured with this cutoff to increase by approximately 50%.

Including only modes where $\eta < 250$, we measure a spectral shot power of $1040 \pm 620 \mu\text{K}^2 \text{ Hz sr}$ for the ACA data, and $770 \pm 340 \mu\text{K}^2 \text{ Hz sr}$ for the ASPECS data, reflecting a modest increase of $\sim 10\%$ in power. This result is consistent with our prior assumption that our measurement is not dominated by galaxies with broad line widths of $\gtrsim 600 \text{ km s}^{-1}$. Though we have not attempted any correction for these effects, we note that if one were to assume that our measurement is solely dominated by objects with line widths of 300 km s^{-1} , we would need to scale up the results presented here by approximately a third.

4.2. Impact of Sample Variance

The values and uncertainties in Table 2 account only for instrumental noise. However, we do expect there to be some intrinsic variance for the relatively small volumes surveyed due to cosmic variance—imprinted by the inhomogeneity of large-scale cosmic structure—and Poisson variance—arising from the discrete number of galaxies within a given volume. We seek here to quantify the effects of both, referring to the combined effects of sample and cosmic variance as “sample variance,” in order to produce a more accurate estimate (and uncertainties) of the true value of $\tilde{I}_s^2(\nu)$ at 100 GHz.

For this analysis, we use simulation results of Keenan et al. (2020), which utilizes the TNG300 simulations from the public data release of Illustris (Nelson et al. 2019) to produce simulated power spectra from ensembles of simulated light cones with realistic large-scale structure. From mock observations that approximately match the ACA and ASPECS data sets, we calculate the distribution of measured shot powers within 1000 light cones, normalized by the “true” shot power, which we estimate by taking the mean of 1000 large (500 arcmin²) light cones. Fixing the relative contributions of the individual lines in our measurement (estimates of which are

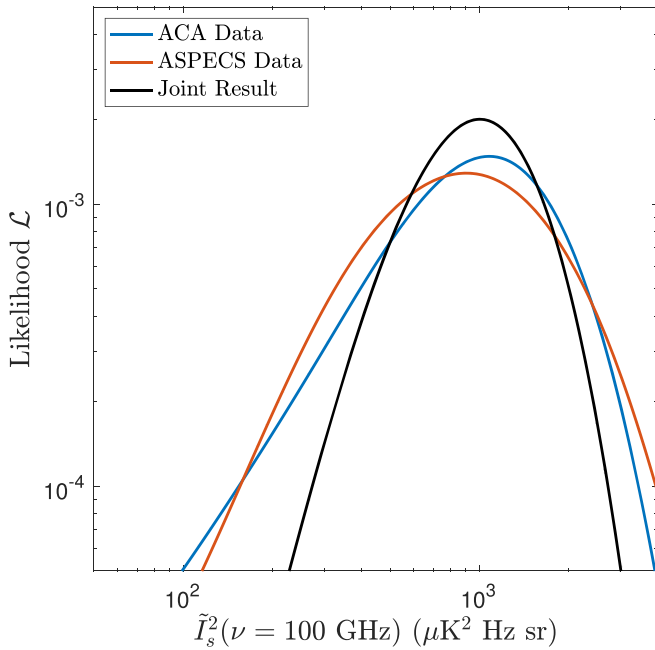


Figure 6. Likelihood estimates of the “true” spectral shot power at 100 GHz, accounting for both the effects of instrument noise and sample variance. The likelihood function from the ASPECS data alone (orange) produce a better constraint on the lower end of the range of estimated spectral shot power relative to that from the ACA data (blue), but a poorer constraint on the upper end. This skew of the ACA likelihood function arises both from the decreased significance of sample variance and the increased instrumental noise. The joint constraint (black) using both data sets is more symmetric, roughly consistent with a log-normal distribution in $\tilde{I}_s^2(\nu)$.

Table 3
Spectral Shot Power Measurements and Uncertainties

Result	Inst. Noise Only	Full Analysis	
		MEDIAN	MLE
ACA	890^{+440}_{-440}	940^{+740}_{-500}	1080^{+850}_{-550}
ASPECS	730^{+240}_{-240}	850^{+850}_{-450}	904^{+890}_{-480}
Joint	770^{+210}_{-210}	960^{+530}_{-370}	1010^{+550}_{-390}

Note. All values are in units of $\mu\text{K}^2 \text{ Hz sr}$.

discussed further in Section 5.1), we construct a probability density functions for measuring a given amount of power in a field of a given size, relative to the “true” spectral shot power. We then run a maximum likelihood estimation (MLE) analysis to calculate the true spectral shot power, given the measurements and uncertainties from the analysis of the ACA and ASPECS data sets. The results of this analysis are reported in Table 3.

The full likelihood functions from our MLE analysis are shown in Figure 6, and the results are reported in Table 3. Combining the results of both data sets together, and accounting for both sample and cosmic variance, we estimate the spectral shot power at 100 GHz to be $\tilde{I}_s^2(\nu) = 1010^{+550}_{-390} \mu\text{K}^2 \text{ Hz sr}$. This “most likely” power is higher than the measured power because, as found in Keenan et al. (2020), the median power measured in small fields is below the true power due to the skewed distribution of power per field. This result is shown on Figure 7, alongside the model predictions described in Section 5.1. We find that, compared to

the set of results that consider the instrument noise only as a source of error, the estimates for spectral shot power have not significantly changed, although the error bars have increased by roughly a factor of 2. This further underscores the importance of accounting for sample variance in the measurements presented here. As the sample variance is closer to log-normal distribution than a normal one, and as it is the dominant source of uncertainty in our measurement, we have evaluated the likelihoods in Figure 6 on logarithmic intervals of $\tilde{I}_s^2(\nu)$. We additionally calculate results for the spectral power in Table 3 using the median of the derived likelihood functions, and with this method we find $\tilde{I}_s^2(\nu) = 960^{+530}_{-370} \mu\text{K}^2 \text{ Hz sr}$, only marginally different than our MLE-derived value.

Finally, we note that in the above analysis, we have assumed that all detected power originates from blindly detected sources, such that no consideration of selection biases is required. However, as the ACA observations targeted the AzTEC-3 source, we note that there may be an excess of CO(5–4) emission measured within the ACA survey volume. As our model predictions for the contribution of this line are low, and the CO(5–4) line AzTEC-3 source contributes only $\sim 1\%$ of the total measured power, we conclude that the effects this potential bias are negligible. The CO(6–5) line of AzTEC-3 is also partially within our frequency coverage and contributes $< 1\%$ of the total measured power.

5. Discussion

5.1. Modeling the Multiple Transitions of CO

As there is some ambiguity as to which line we can ascribe the power measured at 3 mm, we create a simple model to help estimate the amount of power arising from each line species. We adopt the fiducial model of Li et al. (2016), hereafter referred to as L16, with one significant modification to the conversion between infrared and CO luminosity, which is nominally expressed as

$$\log_{10}(L_{\text{IR}}) = a \log_{10}(L'_{\text{CO}}) + b, \quad (11)$$

where L_{IR} is the bolometric infrared luminosity in units of L_{\odot} , and L'_{CO} is the line of the object in units of $\text{K km s}^{-1} \text{ pc}^2$. Rather than using the fiducial values from Carilli & Walter (2013), which is only fit against CO(1–0) luminosities (with $a = 1.37$, $b = -1.74$), we instead adopt the “full sample” correlations from Kamenetzky et al. (2016), which provide fits for the full set of CO rotational lines that may contribute to our measurement. All other parameters match the fiducial model of L16. Star formation rates (SFR) for individual halos are calculated using the model found in Behroozi et al. (2013), assuming a logarithmic scatter of 0.3 dex for the SFR of individual halos, which are converted into infrared luminosities assuming

$$L_{\text{IR}} = 10^{10} \left(\frac{\text{SFR}}{M_{\odot} \text{ yr}^{-1}} \right) L_{\odot}. \quad (12)$$

CO luminosities for individual halos are assumed to have logarithmic scatter of 0.3 dex around the scaling relation in Equation (11). With the exception of halo mass to SFR correlation, each of the aforementioned scaling relationships are assumed to be redshift invariant, which means that the

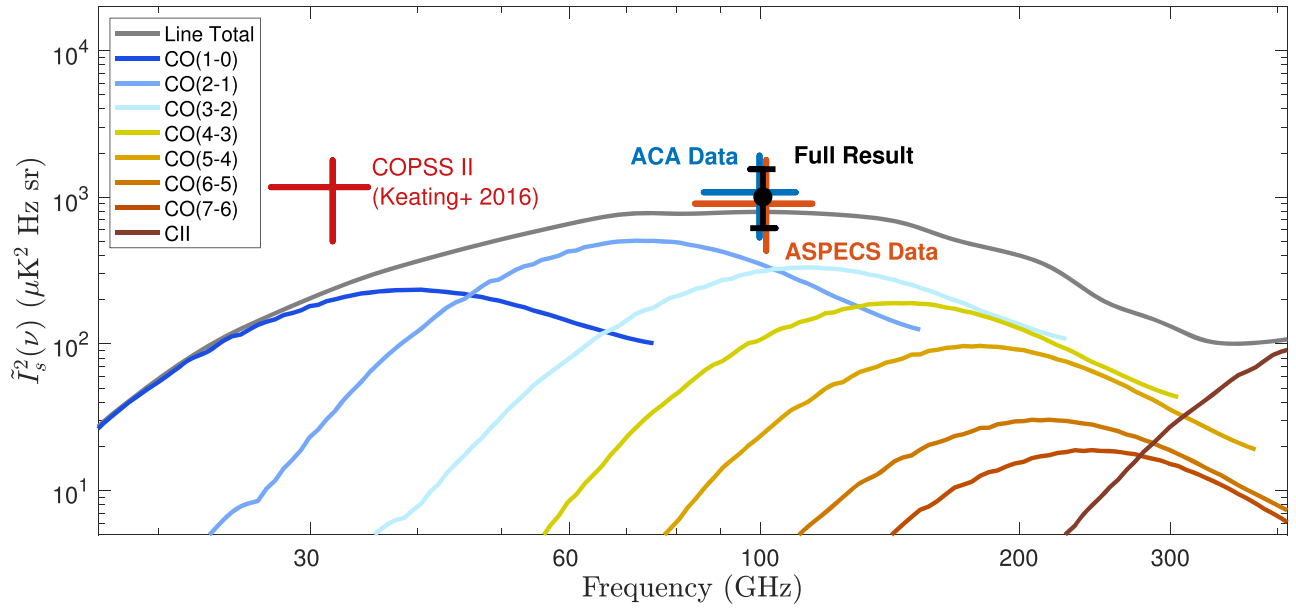


Figure 7. Model estimates for the spectral shot power $\tilde{I}_s^2(\nu)$ —for both individual line species and the cumulative total—as a function of frequency, alongside our measurement-based estimates for the spectral shot power (from Section 4.2). Constraints from the ACA (blue) and ASPECS (orange) data are shown separately, as well as the constraints from the results of our joint analysis for both data sets (black). We find good agreement between the predicted and measured values. Also shown are the constraints from COPSS (red), after correcting for the estimated contributions from clustering power in the measurement (as discussed in Section 5.3). For illustrative effect, we have also included an estimate for the [C II], by using a combination of the L16 model, as well as the model m_1 from Silva et al. (2015).

Table 4
Model Estimates of Spectral Shot Power at 100 GHz

Line Species	$\langle z \rangle$	$P_{\text{shot}}(z)$ ($\mu\text{K}^2 h^{-3} \text{ Mpc}^3$)	$\tilde{I}_s^2(\nu)$ ($\mu\text{K}^2 \text{ Hz sr}$)	f_{total}
CO(2–1)	1.3	100	340	0.43
CO(3–2)	2.5	160	310	0.40
CO(4–3)	3.6	80	120	0.14
CO(5–4)	4.8	20	30	0.03
Total	790	1.00

Note. f_{total} is the fraction of the spectral shot power.

redshift evolution of our model is solely determined by the SFRs, as calculated by Behroozi et al. (2013). Although the connection between star formation and molecular gas is a fairly well-studied phenomenon (e.g., Schmidt 1959; Kennicutt 1998), the redshift evolution of molecular gas is still poorly constrained (Keenan et al. 2020). As the uncertainties in our measurement are significant, we do not expect this to significantly bias the interpretation of our result.

The model estimates of the individual line contributions are shown in Figure 7, over a broad window between 15 and 400 GHz, which approximately spans the range of existing and future measurements targeting CO emission (Crities et al. 2014; Bower et al. 2015; Cleary et al. 2016; K16; Lagache 2018). The model predicts a peak of approximately $800 \mu\text{K}^2 \text{ Hz sr}$ at 100 GHz, which includes contributions from multiple low- J lines from the epoch of peak star formation (Madau & Dickinson 2014). Our model agrees with the measurement presented here to within 20% ($\approx 0.4\sigma$), as shown in Figure 7).

We have also tabulated the spectral shot power of individual line species over the frequency interval of the ACA and ASPECS data (Table 4). These values can then be translated into estimates of the shot power of individual lines by a

minor modification to Equation (10), where

$$P_{\text{shot,line}}(z) \approx f_{\text{total}} X(z)^2 Y(z, \nu_{\text{rest,line}}) \tilde{I}_s^2(\nu). \quad (13)$$

Over the frequency interval of our measurement, our model predicts that the CO(2–1) and CO(3–2) rotational lines will contribute approximately equal amounts of power. The power contribution of the CO(4–3) lower by roughly two-thirds compared to the lower- J lines, while CO(5–4) is lower by about an order of magnitude. Higher- J lines are expected to only contribute a marginal amount of power relative to these three line species, with the sum of all contributions where $J_{\text{upper}} \geq 6$ equal to less than 1% of the predicted power. We will therefore neglect the contributions of these lines, and assume that only CO(2–1), CO(3–2), CO(4–3), and CO(5–4) emission are present in our measurement. We also find that these estimates are in rough agreement with the the luminosity function fits derived from direct detection measurements made with ASPECS (Decarli et al. 2019; Uzgil et al. 2019), with respect to CO(2–1) and CO(3–2) contributing the bulk of the spectral shot power, followed by CO(4–3).

In our estimates of f_{total} , we have excluded the CO(1–0) line from consideration. While the estimated shot power of this line at 100 GHz relatively low, where $P_{\text{shot,CO(1-0)}} \sim 1 \mu\text{K}^2 h^{-3} \text{ Mpc}^3$, the spectral shot power it contributes is much more significant, with $\tilde{I}_s^2(\nu) = 230 \mu\text{K}^2 \text{ Hz sr}$. The reason for the apparent discrepancy lies in the normalization term $X^2 Y$ in Equation (10), which shrinks to zero as the redshift approaches zero. This feature is a natural consequence of the inverse square law, where relatively faint objects at small luminosity distances can have similar integrated line fluxes as a brighter object at greater distance. For large-area surveys, CO(1–0) would likely be a significant part of the measured spectral shot power. However, for both the ASPECS and ACA data sets, we would expect that the objects dominating the spectral shot power would have line luminosities of $L_{\text{CO(1-0)}} \sim 10^9 - 10^{10} \text{ K km s}^{-1} \text{ pc}^2$, which

Table 5
Estimates of Shot Power for Various CO Line Species

Line Species	$\langle z \rangle$	k_{\min}^a ($h \text{ Mpc}^{-1}$)	k_{\max}^b ($h \text{ Mpc}^{-1}$)	V_{surv}^c (10^3 Mpc^3)	$\tilde{I}_s^2(\nu)$ ($\mu\text{K}^2 \text{ Hz sr}$)	$P_{\text{shot}}(z)$ ($\mu\text{K}^2 h^{-3} \text{ Mpc}^3$)	$P_{\text{shot,CO}(1-0)}(z)$ ($\mu\text{K}^2 h^{-3} \text{ Mpc}^3$)
CO(2–1)	1.3	6	230	22	430_{-170}^{+230}	120_{-50}^{+70}	205_{-90}^{+140}
CO(3–2)	2.5	4	160	39	400_{-150}^{+220}	210_{-80}^{+110}	1140_{-500}^{+870}
CO(4–3)	3.6	3	130	49	150_{-60}^{+80}	100_{-40}^{+50}	950_{-440}^{+800}
CO(5–4)	4.8	3	120	54	30_{-10}^{+20}	20_{-10}^{+10}	440_{-200}^{+350}

Notes.

^a Minimum wavenumber k for which our measurements have meaningful sensitivity, defined as being within a factor of 0.5 dex (~ 3) of the peak sensitivity of our power spectrum at a given redshift.

^b Maximum wavenumber k for which our measurements have meaningful sensitivity.

^c Total volume surveyed, summed across both ACA and ASPECS observations.

would be readily detected in imaging of both sets of data. As no such sources are found, we conclude that our power spectrum measurement does not have a significant contribution from CO(1–0) and have thus excluded it from our analysis for the sake of clarity.

5.2. Power Spectrum Estimates of Individual Lines

To better compare with previously published results, we estimate the individual contributions of each line to $\tilde{I}_s^2(\nu)$, based on the results of our the modeling efforts discussed in Section 5.1. More specifically, we have used our derived values of f_{total} (reported in Table 4) to estimate the power of each individual lines. Results from this analysis are reported in Table 5, which show the estimated shot power for each line to be of order $\sim 100 \mu\text{K}^2 h^{-3} \text{ Mpc}^3$. With these values, we now seek to estimate the shot power of the CO(1–0) line at a range of redshifts, using an appropriate set of line ratios, $r_{J,1}$, where we assume that

$$P_{\text{shot,CO}(J-J-1)} = r_{J,1}^2 P_{\text{shot,CO}(1-0)}, \quad (14)$$

where J refers to the upper-level rotational state of CO. We adopt here the set is presented in Daddi et al. (2015), who used measurements of optically selected (BzK) galaxies at $z = 1.5$ to estimate the relative line ratios of “normal” star-forming galaxies at high redshift. The derived line ratios for $J = 2, 3, 4, 5$ are $r_{J,1} = 0.76 \pm 0.09, 0.42 \pm 0.07, 0.31 \pm 0.06, 0.23 \pm 0.04$, respectively.⁵ The resulting estimates are shown in Table 5. We have used the Daddi et al. (2015) line ratios in place of those from Kamenetzky et al. (2016), as the former is derived from a sample of high-redshift objects, whereas the latter is derived from low-redshift galaxies. We find similar results when using the “non-ULIRG” L_{IR} to L'_{CO} correlation from Kamenetzky et al. (2016) in our model, with agreement of order 10%–20% between the two sets of line ratios.

5.3. Comparison to COPSS II

In K16, it was assumed that all power measured was attributable to shot power only, as several models (e.g., Visbal & Loeb 2010; Lidz et al. 2011; Pullen et al. 2013) had suggested that the contributions of large-scale structure in the power spectrum would be negligible over the spatial scales that COPSS was most sensitive to ($k = 0.5\text{--}2 h \text{ Mpc}^{-1}$). However,

more recent models (e.g., L16) and our own simulations (Keenan et al. 2020) indicate that the clustering contribution to the COPSS power should not be ignored.

Rather than attempting to use approximate astrophysical models, we can use the linear matter power spectrum itself to estimate the contributions from large-scale structure. The power spectrum, $P(k, z)$, as measured in an intensity mapping analysis can be written as

$$P(k, z) = \langle T_b(z) \rangle^2 b^2(z) P_{\text{lin}}(k, z) + P_{\text{shot}}(z), \quad (15)$$

where P_{lin} is the linear matter power spectrum, $b(z)$ is the luminosity-weighted halo bias, and $\langle T_b(z) \rangle$ is the mean brightness temperature of the line being examined at a given redshift. In Equation (15), the $\langle T_b(z) \rangle^2 b^2(z) P_{\text{lin}}(k, z)$ component is the power arising from the induced clustering of CO emitters from large-scale structure. We further define the halo bias as

$$b(z) = \frac{\int_{M_{\min}}^{\infty} dM L(M) \frac{dn}{dM} b(M, z)}{\int_{M_{\min}}^{\infty} dM L(M) \frac{dn}{dM}}, \quad (16)$$

where $b(M, z)$ is the mass-dependent halo bias, and $L(M)$ is the luminosity for a halo of mass M . Halos with masses below the low-mass limit, M_{\min} , are assumed to be deficient in line emission. With a choice of linear power spectrum appropriate for the redshift range of COPSS (Lewis et al. 2000; Murray et al. 2013), we solve for the individual components of Equation (15) using the COPSS power spectrum, fitting for P_{shot} and $\langle T_b(z) \rangle^2 b^2(z)$ for CO(1–0). We perform a likelihood analysis for both parameters, requiring only that both components be positive, and evaluating the χ^2 value for a given set of parameters against the power spectrum presented in K16. The results of this analysis are shown in Figure 8.

Marginalizing over the $\langle T_b(z) \rangle^2 b^2(z)$ term—which we have only weak constraints for—we estimate the shot power of CO(1–0) at $z = 2.6$ to be $P_{\text{shot}}(z) = 2000_{-1200}^{+1100} \mu\text{K}^2 h^{-3} \text{ Mpc}^3$. We have shown this result alongside those from our analysis of the ACA and ASPECS data set in Figure 7. We note that the estimated shot power of the COPSS measurement exceeds the model prediction by nearly a factor of 5. However, the error bars on the COPSS measurement are large, such that the discrepancy between model and measurement is approximately 1.4σ , which is of limited statistical significance.

While not shown in Figure 7, we note the discrepancy between COPSS and our model is virtually eliminated when

⁵ The value for $r_{4,1}$ is based on an interpolation originally performed in Decarli et al. (2016).

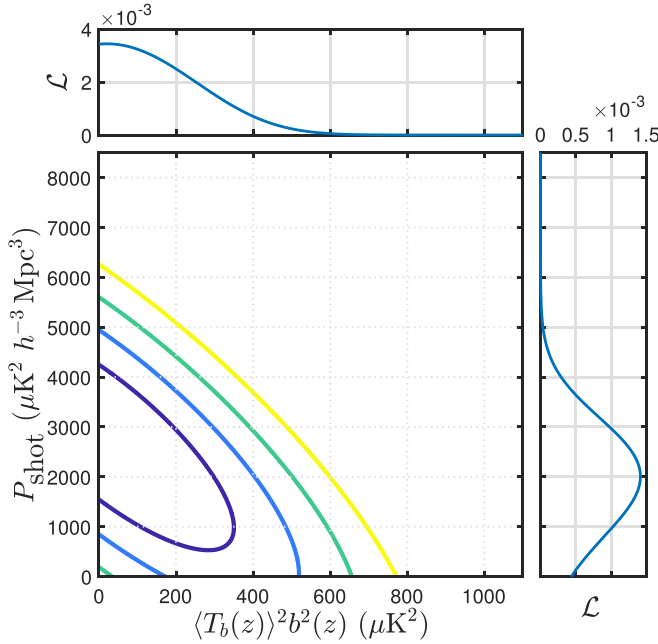


Figure 8. The χ^2 statistic for our power spectrum fit of the COPSS CO(1–0) power spectrum measurement, along with the marginalized likelihoods for the individual power spectrum components for P_{shot} and $\langle T_b(z) \rangle^2 b^2(z)$. Center: the results of the joint fit for the shot power of CO(1–0) and $\langle T_b(z) \rangle^2 b^2(z)$ are shown, with contours outlining $\Delta\chi^2 = 1, 2.3, 4, 6.2$ relative to the minimized χ^2 value. There is significant covariance between the fits for the two parameters, which are a result of a relatively small number of bins at $k < 1 \, h \, \text{Mpc}^{-1}$ constraining the cluster power component of the power spectrum. Right: the marginalized likelihood for P_{shot} . As a result of our analysis, we provide a refined estimate for CO(1–0) of $P_{\text{shot}} = 2000^{+1100}_{-1200} \, \mu\text{K}^2 \, h^{-3} \, \text{Mpc}^3$ at $z = 2.6$. We note that if we set $\langle T_b(z) \rangle^2 b^2(z) = 0$, we recover the original K16 estimate of $3000 \, \mu\text{K}^2 \, h^{-3} \, \text{Mpc}^3$. Top: the marginalized likelihood for $\langle bT \rangle^2$. Due to the limited signal-to-noise within the COPSS measurement, we are only able to put an upper limit for CO(1–0) of $\langle T_b(z) \rangle^2 b^2(z) < 420 \, \mu\text{K}^2$ at $z = 2.6$ (95% confidence). With an appropriate choice of halo-mass function (Tinker et al. 2008, 2010) and estimate for $L(M)$ for CO (L16), we can translate this into an upper limit for the brightness temperature of the CO(1–0) line at $z = 2.6$ of $T_b < 8.2 \, \mu\text{K}$ (95% confidence).

using the $L_{\text{IR}} - L_{\text{CO}}$ scaling relationship derived from the “non-ULIRG” sample from Kamenetzky et al. (2016), although it does raise the expected spectral shot power at 100 GHz by approximately a factor of 3, which creates tension with our current measurement.

5.4. Comparison to other Blind Surveys for CO Emission

We now compare our result to other blind line detection surveys. Using the luminosity functions presented in Decarli et al. (2019), Uzgil et al. (2019) estimated the spectral shot power at 100 GHz to be $\tilde{I}_s^2(\nu) = 610^{+1040}_{-330} \times 10^2 \, \mu\text{K}^2 \, \text{Hz sr}$. This value is in good agreement with those derived here, noting that while the measurement presented in this paper is greater by roughly 50%, both are within the limits of their respective uncertainties. We note that our result is in moderate tension with the power spectrum results of Uzgil et al. (2019), who found $\tilde{I}_s^2(\nu) = -930 \pm 610 \, \mu\text{K}^2 \, \text{Hz sr}$ (excluding the results for $k \geq 60 \, h \, \text{Mpc}^{-1}$, for reasons discussed in Appendix B). The difference is larger than what one might expect, as both analyses utilize the ASPECS data set. However, we note that two results were generated using separate reduction pathways, including different flagging schemes and power spectrum estimators. Neglecting corrections for sample variance effects, we find our results from the ASPECS data set are reasonably close to the

estimated minimum found in Uzgil et al. (2019) by summing the power contributions of all sources detected at high confidence (shown in Table 2 of González-López et al. 2019), where $\tilde{I}_s^2(\nu) > 500 \, \mu\text{K}^2 \, \text{Hz sr}$, and similarly find our results (prior to correction for sample variance effects) are below their 3σ power spectrum upper limit, where $\tilde{I}_s^2(\nu) < 890 \, \mu\text{K}^2 \, \text{Hz sr}$.

The Plateau de Bure High- z Blue Sequence Survey 2 (PHIBSS2; Lenkic et al. 2020) provides another set of serendipitous galaxy detections. A calculation of the estimated spectral shot power from the PHIBSS2 source catalog is difficult due to the highly uneven depths of individual pointings and the wide spread of frequencies over which the data were taken. However, as a comparison by proxy, we note that the measured number density of bright CO(3–2) objects appears to be fairly well matched to the derived CO(1–0) luminosity function in K16, assuming $r_{3,1} = 0.42$. That both surveys see such objects may be a by-product of the relatively large sky areas covered by both measurements and thus less sensitive to the effects of sample variance.

Though less direct than the comparison with ASPECS, we also compare our results here to those from the CO Luminosity Density at High- z (COLDz) survey (Pavesi et al. 2018). In analyzing the fitted luminosity functions from COLDz, Uzgil et al. (2019) estimated the CO(1–0) shot power at $z = 2.4$ to be $P_{\text{shot,C}} = 270 \, \mu\text{K}^2 \, h^{-3} \, \text{Mpc}^3$, which is in marginal agreement with what we estimate in Section 5.2. This may be the result of sample variance between the fields surveyed (Keenan et al. 2020).

5.5. Constraints on Cosmic Molecular Gas Abundance

Having derived estimates for the CO(1–0) shot power at a range of redshifts, we now seek to translate these into constraints on the cosmic molecular gas density, $\rho_{\text{H}_2}(z)$. To do so, we note that several works have found that the fractional mass of molecular gas within a given halo, f_{H_2} , appears to peak at $M_{\text{halo}} \approx 10^{12} \, M_{\odot}/h$ (Lagos et al. 2011, 2015; Popping et al. 2015), approximately the virial mass of the Milky Way (Watkins et al. 2019)—which appears to be redshift invariant. For halos below this mass limit, f_{H_2} is estimated to scale in near-linear fashion with halo mass. Based on these theoretical findings, we estimate that the CO(1–0) luminosity of a given halo can be approximated by

$$L_{\text{CO}}(M) = A_{\text{CO}} \frac{M^2}{M_0}; \, M \leq M_0 \quad (17)$$

$$L_{\text{CO}}(M) = A_{\text{CO}} M_0; \, M \geq M_0. \quad (18)$$

In Equation (17), M is the halo mass, $L_{\text{CO}}(M)$ is the expected CO(1–0) luminosity for a halo of a given mass, A_{CO} is the mass to CO(1–0) luminosity ratio for halos of mass M_0 , where we have set $M_0 = 10^{12} \, M_{\odot} \, h^{-1}$. In effect, the luminosities of halos scale as M^2 up to M_0 , above which halos are assumed to have approximately equal luminosity. This scaling relationship is similar to that found in L16, as well as that effectively assumed for our adapted model in Section 5.1.

Using the fiducial values from L16 for the scatter between halo mass and CO luminosity, and utilizing the halo-mass functions of Tinker et al. (2008, 2010), we are able to fit for the value of A_{CO} using the CO(1–0) estimates using the Daddi et al. (2015) estimates for the CO line ratios. Assuming a value $\alpha_{\text{CO}} = 3.6 \, M_{\odot} \, (\text{K km s}^{-1} \, \text{pc}^2)^{-1}$, we are able to translate the

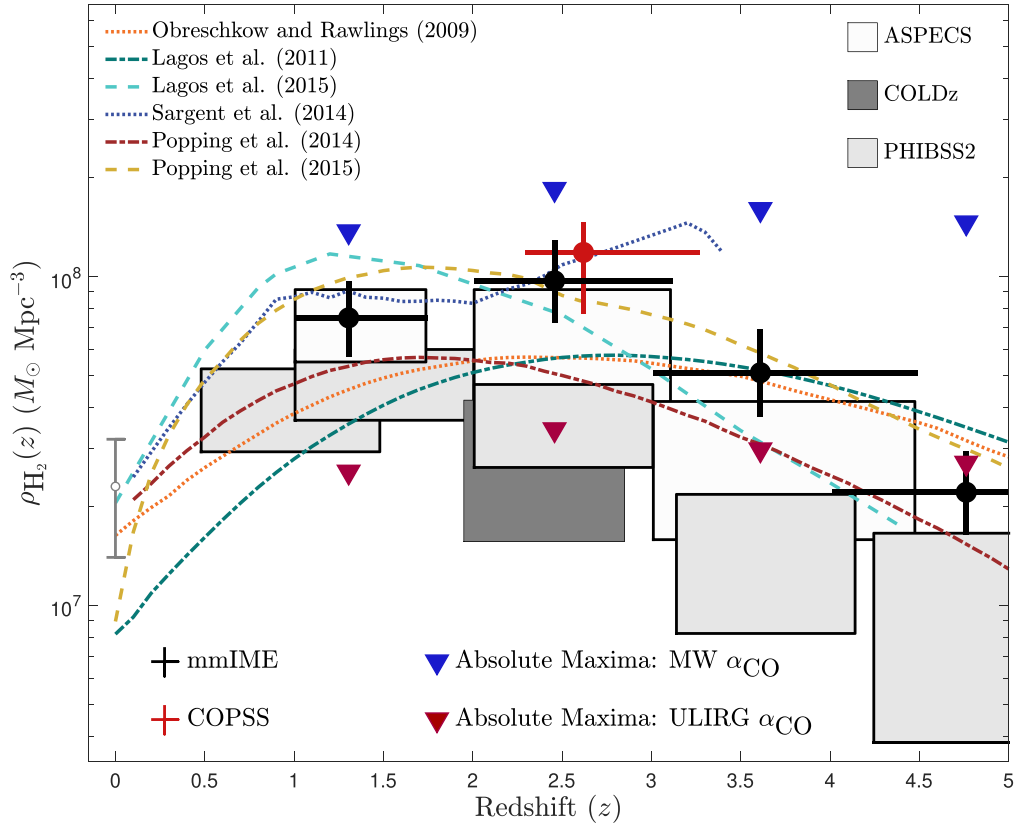


Figure 9. Constraints on the cosmic molecular gas density as a function of redshift. The results from the analysis presented here (black) are in good agreement with those from COPSS (red) and ASPECS (white boxes), although they reside somewhat higher than estimates from PHIBSS2 (light gray boxes) and COLDz (dark gray boxes). A constraint at $z \approx 0$ (open circle) from Keres et al. (2003) is also shown. For each redshift bin, we show the maximum power for that redshift assuming that all measured power comes from that redshift bin, using the Milky Way conversion between luminosity and gas mass (see text; blue triangles), the same assumption made to place the black points, and the same limit assuming a ULIRG-like conversion (red triangles). For comparison, an ensemble of theoretical models for $\rho_{H_2}(z)$ are shown: Obreschkow & Rawlings (2009) is shown as a dotted orange line, Lagos et al. (2011) is shown as a dotted-dashed green line, Lagos et al. (2015) is shown as a dashed teal line, Sargent et al. (2014) is shown as a dotted blue line, Popping et al. (2014) is shown as dotted-dashed brown line, and Popping et al. (2015) is shown as a dashed yellow line. The constraints presented here are in broad agreement with this ensemble of models, although constraints at $z = 2.5$ reside at the top end of the range of predictions.

CO luminosities from Equation (17) into molecular gas masses, and integrating over all halo masses, are able to provide an estimate for $\rho_{H_2}(z)$. The results from this analysis are reported in Table 6 and shown in Figure 9.

As there is some ambiguity as to how much emission is truly arising from each redshift window, we calculate an additional set of estimates, where we assume that *all* of the power measured originates from a single spectral line at a given redshift, using the Daddi et al. (2015) line ratios to generate an estimate for CO(1–0). With these absolute maxima, we consider two separate scenarios to further assist in our interpretation of the data. For the first, which we refer to as the “all MW” scenario, we adopt the Milky Way value for α_{CO} , where $\alpha_{CO,MW} = 4.3 M_\odot (\text{K km s}^{-1} \text{ pc}^2)^{-1}$ (Frerking et al. 1982; Dame et al. 2001; Bolatto et al. 2013). In the second, which we refer to as the “all ULIRG” scenario, we adopt the value of α_{CO} found from observations of local ULIRGs, where $\alpha_{CO,ULIRG} = 0.8 M_\odot (\text{K km s}^{-1} \text{ pc}^2)^{-1}$ (Downes & Solomon 1998). These results are also reported in Table 6 and shown in Figure 9.

Comparing our results to theoretical estimates, we find that the mmIME data points are comparable to the theoretical models, except at $z \approx 2.5$, where mmIME is higher than all but one model. Our maxima from the all-MW estimates lie well above the ensemble of models. This would appear to place a cap of $\rho_{H_2}(z) \lesssim 2 \times 10^8 M_\odot \text{ Mpc}^{-3}$ across all of cosmic time.

Table 6
Estimates of the Cosmic Molecular Gas Density

$\langle z \rangle$	Redshift Range	$\rho_{H_2}(z)$ ($10^7 M_\odot \text{ Mpc}^{-3}$)	Absolute Maximum ^a	
			(10 ⁷ $M_\odot \text{ Mpc}^{-3}$)	
			All MW ^b	All ULIRG ^c
1.3	1.0–1.7	$7.5^{+2.2}_{-1.8}$	13.7	2.5
2.5	2.0–3.1	$9.7^{+3.2}_{-2.5}$	18.4	3.4
3.6	3.0–4.5	$5.1^{+1.8}_{-1.3}$	16.0	3.0
4.8	4.0–5.8	$2.2^{+0.7}_{-0.6}$	14.8	2.7
2.6	2.3–3.3	$11.8^{+2.8}_{-4.1}$

Notes.

^a Assumes all emission arises from a single redshift window.

^b Uses $\alpha_{CO} = 4.3 M_\odot (\text{K km s}^{-1} \text{ pc}^2)^{-1}$.

^c Uses $\alpha_{CO} = 0.8 M_\odot (\text{K km s}^{-1} \text{ pc}^2)^{-1}$.

Comparing our results against those previous experiments, we find that our estimates lie above those from COLDz and PHIBSS2, being more consistent with ASPECS. We find very good agreement between mmIME, ASPECS, and COPSS at $z \approx 2.5$, with all three values clustered around $10^8 M_\odot \text{ Mpc}^{-3}$. The discrepancy with the PHIBSS2 data could result from

incompleteness in their variable-depth survey. Lenkić et al. (2020) do not account for sources below their detection threshold, which may include L^* galaxies at $z > 2$. We also find that COLDz estimates are also well below those presented here.

We particularly note the large spread in results at $z \approx 2-3$, where the present measurements (and their associated 1σ error intervals), stretch over an order of magnitude. That the intensity mapping-derived constraints lie above those from direct detection suggest that such measurements may be capturing emission from galaxies below direct detection threshold. This possibility is explored in Keenan et al. (2020) and is a serious concern of Popping et al. (2019).

6. Conclusion

We have presented the first results from mmIME, an intensity mapping experiment targeting cool-gas tracers in the millimeter-wave regime. We have utilized data designed for conducting blind surveys at 3 mm, over an approximate total survey volume of 10^5 Mpc^3 , finding the following results:

1. We report a measurement of $730^{+240}_{-240} \mu\text{K}^2 \text{ Hz sr}$ (99.9% confidence) in our analysis of the ASPECS 3 mm data set (González-López et al. 2019) and a measurement of $890^{+440}_{-440} \mu\text{K}^2 \text{ Hz sr}$ (97.8% confidence) in our analysis of an ACA 3 mm data set collected on a region within the COSMOS field. Accounting for sample variance effects, we estimate the spectral shot power at 100 GHz to be $\tilde{I}_s^2(\nu) = 1010^{+550}_{-390} \mu\text{K}^2 \text{ Hz sr}$, rejecting the zero-power hypothesis ($\tilde{I}_s^2(\nu) = 0$) to 99.99% confidence. We find that these results are in good agreement with an expanded version of a model first presented in L16, using the $L_{\text{IR}} - L'_{\text{CO}}$ scaling relationships measured in Kamenetzky et al. (2016).
2. Using the aforementioned model, we have produced estimates of the shot power at 100 GHz for CO(2–1), CO(3–2), CO(4–3), and CO(5–4) of $P_{\text{shot}} = 120^{+80}_{-40}$, 200^{+120}_{-70} , 90^{+70}_{-40} , and $20^{+10}_{-10} \mu\text{K}^2 h^{-3} \text{ Mpc}^3$, respectively.
3. Using a set of line ratios appropriate for normal, Milky Way-like galaxies at high redshift (Daddi et al. 2015), we produced estimates of the CO(1–0) shot power at $z = 1.3, 2.5$, and 3.6 . We find good agreement between these values and a refined estimate of the shot power from COPSS of $2000^{+1100}_{-1200} \mu\text{K}^2 h^{-3} \text{ Mpc}^3$.
4. We set constraints on the cosmic molecular gas density between $z \approx 1-5$, finding $\rho_{\text{H}_2}(z) = 7.5^{+2.2}_{-1.8} \times 10^7$, $9.7^{+3.2}_{-2.5} \times 10^7$, and $5.1^{+1.8}_{-1.3} \times 10^7 M_{\odot} \text{ Mpc}^{-3}$ for $z = 1.3, 2.5$, and 3.6 , respectively. For $\rho_{\text{H}_2}(z \approx 3)$, we find good agreement with the results of COPSS and ASPECS.

While intriguing, the results presented here will likely require further observational follow-up, particularly as the uncertainties on our measurement are significant. Fortunately, further constraints from intensity mapping experiments targeting CO are on the horizon. The SMA is presently engaged in intensity mapping-focused observations as part of mmIME, targeting aggregate CO emission in the 1.3 mm atmospheric window. The ASIAA Intensity Mapping of CO (Bower et al. 2015) project will similarly target lines in the 3 mm window, with prospects for cross-correlation with measurements from COPSS. The CarBON C II line in post-reionization and ReionizaTiOn epoch project (Lagache 2018) will, among other

things, make power spectrum measurements at 2 and 1.3 mm, likely probing a similar a set of lines similar to what we have examined here. Similarly, the Tomographic Ionized-carbon Mapping Experiment (Crites et al. 2014), while targeting [C II] emission at $z \approx 6-10$, will also be capable of measuring CO in the 1.3 mm atmospheric window. Finally, the CO Mapping Array Pathfinder (Cleary et al. 2016) will measure the CO(1–0) line at $z \approx 2.5$, with access to much larger spatial scales than were originally measured in COPSS.

There is significant potential for intensity mapping experiments of CO and [C II] for probing the astrophysics of the gas fueling the star formation within early galaxies. Numerous theoretical studies have evaluated the potential of such experiments for placing constraints on cosmology (e.g., Fonseca et al. 2017; Bernal et al. 2019), covering a variety of topics from the expansion history of the early Universe (Karkare & Bird 2018) to the physics of inflation (Moradinezhad Dizgah et al. 2019). Such experiments are likely to benefit from the decades of significant technical and observational studies of the CMB, and may be highly compatible with future experiments targeting the CMB (e.g., Switzer 2017; Delabrouille et al. 2019; Moradinezhad Dizgah & Keating 2019).

The authors would like to thank the anonymous referee for their timely and thoughtful feedback, which helped improve the quality of this manuscript. We thank T. Li for his contributions and collaboration in this earliest stages of this work. We thank S. Paine for his assistance in identifying atmospheric features and F. Fornasini for her feedback on several figures prepared for this manuscript. We thank N. Mashian, T.-C. Chang, A. Fialkov, and A. Loeb for the many useful discussions on theoretical aspects related to this work. GKK would additionally like to several members on the intensity mapping community who provided thoughtful feedback and useful conversations over the course of this project, including P. Breyse, P. Bull, D. Chung, A. Crites, A. Dizgah, O. Doré, K. Karkare, A. Pullen, and G. Sun.

This paper makes use of the following ALMA data: ADS/JAO.ALMA #2013.1.00146.S, ADS/JAO.ALMA #2016.1.00324.L, ADS/JAO.ALMA #2016.1.01149.S, and ADS/JAO.ALMA #2018.1.01594.S. ALMA is a partnership of ESO (representing its member states), NSF (USA) and NINS (Japan), together with NRC (Canada), MOST and ASIAA (Taiwan), and KASI (Republic of Korea), in cooperation with the Republic of Chile. The Joint ALMA Observatory is operated by ESO, AUI/NRAO and NAOJ. The National Radio Astronomy Observatory is a facility of the National Science Foundation operated under cooperative agreement by Associated Universities, Inc. D.P.M. and R.P.K. were supported by the National Science Foundation through CAREER grant AST-1653228. R.P.K. was supported by the National Science Foundation through Graduate Research Fellowship grant DGE-1746060.

Appendix A

Impact of Line Widths and Instrument Resolution

The design of intensity mapping experiments, and the interpretation of observational data as three-dimensional power spectra, must consider the impact of internal galaxy motions on the intensity mapping power spectrum. Galaxy rotation, turbulence, and mergers spread the line emission in redshift space over hundreds of km s^{-1} . Because radial velocity is mapped to distance through the Hubble flow, this width corresponds to Mpc of radial distance, and therefore an attenuation of power in modes where $k \gtrsim 0.1 \text{ Mpc}^{-1}$. As several planned intensity mapping

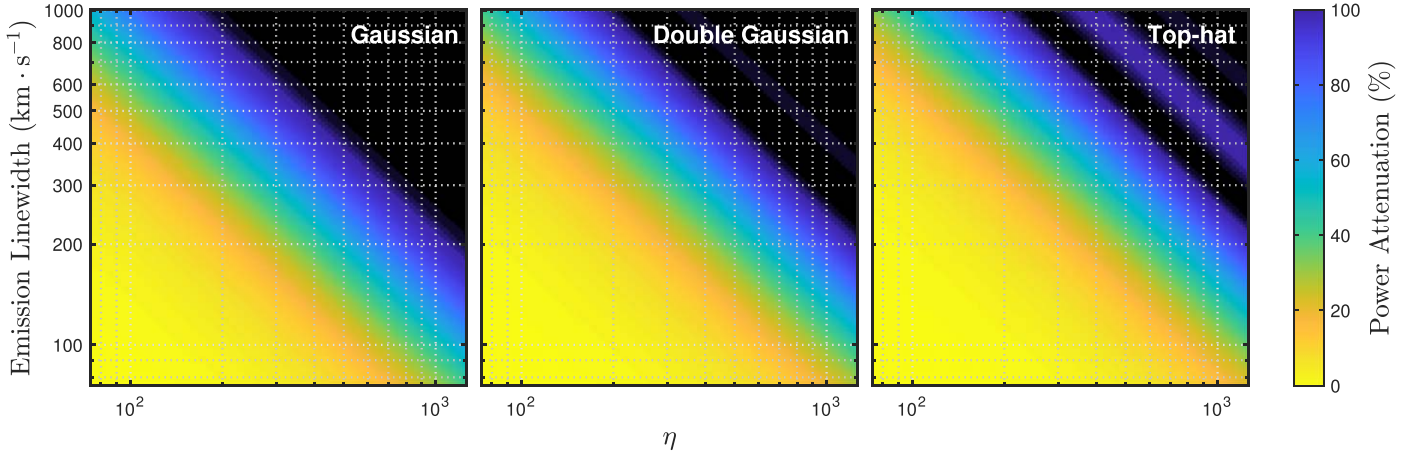


Figure A1. Estimated attenuation of power as a function of emission line width and η . Typically, the power is attenuated by half when $\eta \sim c/2\Delta v_{\text{line}}$. We note that the attenuation here is shown on a per-halo basis, and thus most appropriate for calculations of the shot power, although similar attenuation will be seen in the clustering component of the power spectrum. At $\eta \approx 130$ –190 (depending on line profile type), the attenuation in power is $\approx 50\%$ for $\sigma_{\text{line}} = 616 \text{ km s}^{-1}$, the maximum line width found in González-López et al. (2019).

experiments will have at least some sensitivity to this range in k , we consider here the impact of such effects here.

A.1. Impact of Realistic Line Emission Profiles

For this analysis, we represent galaxies as three different velocity profiles: top-hat, Gaussian, and double-Gaussian. The flux density for a top-hat line profile is assumed a constant nonzero value over a velocity range defined by the line width, Δv_{line} , and zero outside of this range. For the Gaussian line profile, we set the FWHM of the profile to be Δv_{line} . The double-Gaussian line profile is defined as

$$S_{\text{line}}(\Delta v_{\text{line}}, \Delta v) = A(e^{((B\Delta v - \Delta v_{\text{line}})/\Delta v_{\text{line}})^2} + e^{((B\Delta v + \Delta v_{\text{line}})/\Delta v_{\text{line}})^2}), \quad (\text{A1})$$

where Δv is the velocity offset from line center, and A and B are normalization constants, where A is set by the line luminosity of the object and $B = 3.6421$. This represents two equal Gaussians of $\text{FWHM} \approx \Delta v_{\text{line}}/2$, spaced roughly $\Delta v_{\text{line}}/2$ apart.

Shown in Figure A1 is the attenuation for a given line width for the three line profiles as a function of wavenumber η . Generally speaking, modes with significant attenuation reside at $\eta \gtrsim 100$, with the Gaussian line profile showing generally more attenuation than the top-hat line profile at a given value of η and Δv_{line} , and the double-Gaussian attenuation generally found between the two. Based on the modeling of L16, we expect galaxies within halos of $\sim 10^{12} M_{\odot}$ to provide the bulk of the aggregate line emission for CO in particular, and are estimated to have line widths of $\sim 300 \text{ km s}^{-1}$ (Obreschkow et al. 2009), which will be attenuated by 50% at $\eta \approx 450$. Our analysis of the ACA and ASPECS data sets exclude $\eta > 500$ modes to reduce the impact of this line attenuation. Integrating across all wavenumbers used in the analysis of the ASPECS and ACA data, we estimate that the band-averaged power is attenuated by $\sim 25\%$ for emitters with line widths of 300 km s^{-1} and $\sim 50\%$ for emitters of 600 km s^{-1} . These losses drop to $\sim 10\%$ and $\sim 25\%$, respectively, when only

including modes where $\eta < 250$. Without a model distribution of line widths, we choose not to make any correction for this effect in our power spectrum.

A.2. Impact of Channel Resolution

We now turn to the impact of the instrumental spectral resolution on line intensity mapping measurements. We run separate trials using each of the line profiles mentioned above, generating a mock catalog of sources with fixed Δv_{line} and random sky position and center frequency. We then generate an image cube, simulating the expected emission to be found within each voxel for a given channel resolution, Δv_{chan} , expressed in velocity units.

The results of our analysis are shown in Figure A2. In general, we find that the recovered power decreases at all values of η with increasing Δv_{chan} . For a band-averaged value across all accessible values of η , we find that the losses are most significant when $\Delta v_{\text{chan}} \sim \Delta v_{\text{line}}$, where the recovered power is $\approx 85\%$ of what one would expect given $\Delta v_{\text{chan}} \ll \Delta v_{\text{line}}$. With decreased resolution (i.e., $\Delta v_{\text{chan}} > \Delta v_{\text{line}}$), the band-averaged losses in power are somewhat diminished, although can still produce losses of order $\sim 5\%$. For the analysis presented in Section 4 (where $\Delta v_{\text{chan}} \sim 0.1\Delta v_{\text{line}}$), we estimate the loss in band-averaged power due to instrument resolution effects to be $\lesssim 1\%$.

We note here that we have adopted a simple top-hat function for the spectral PSF, rather than something more closely related to the typical output on an instrument (e.g., a sinc or sinc^2 function for an interferometer). We have done so in part because for the data sets discussed in Section 2, the native spectral resolution of the data is quite fine, such that the width of the PSF is quite small relative to the line widths in question. In averaging down the data for analysis, our resultant PSF resembles something fairly close to a top-hat function. Accounting for the impact of the spectral PSF is an instrument-specific task, though we note that with few exceptions, most are likely to see similar losses in the high- η modes.

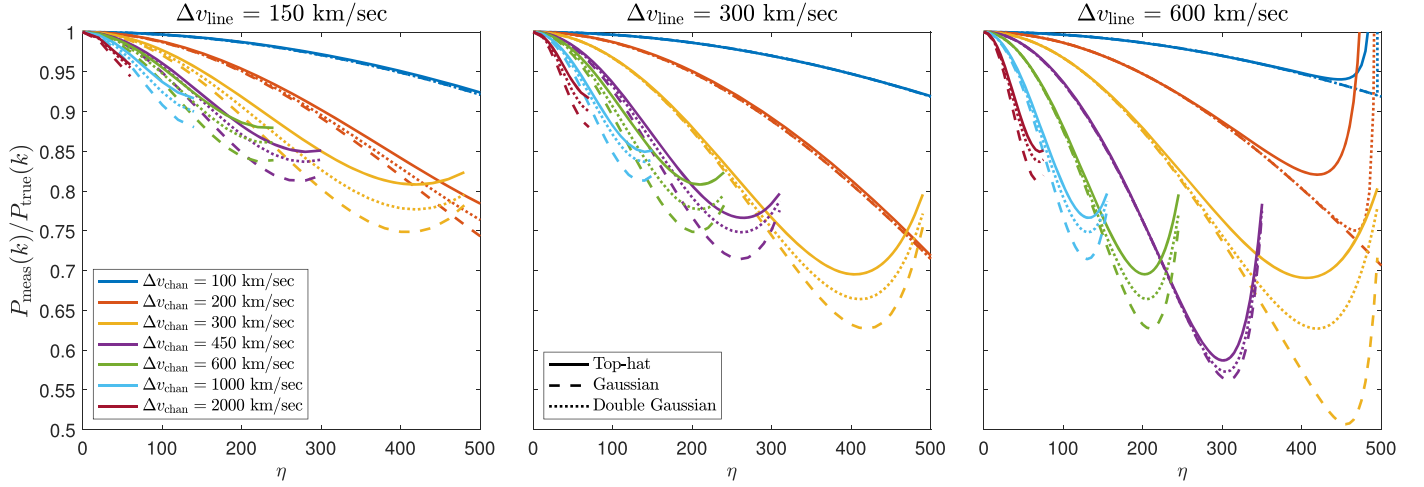


Figure A2. Power recovered in the presence of instrument resolution effects and non-infinitesimal line widths. In the figures above, power has been averaged over each plane of constant η and normalized by estimated power in the absence of channel resolution effects. In the right-most panel, some spectra show a significant increase in power at very high values of η . This can be attributed to the combination of aliasing and the low power intrinsically present in these modes (as shown in Figure A1).

Appendix B

Image-domain Power Spectrum Analysis with Interferometers

The power spectrum analysis presented in this paper works in the visibility domain that is the natural output of interferometric measurements. In this space, the Fourier dual of the image domain, the noise is well understood and uncorrelated between measurements. Each visibility also naturally represents a specific Fourier component, which makes the mapping to the power spectrum measurement very simple.

Of course, interferometric observations are most often converted to image space for scientific interpretation and so it is worth considering the path through the image domain to a power spectrum. In particular, this approach was used in the Uzgil et al. (2019) analysis of the ASPECS data to measure the CO power spectrum. They report $P(k)_{\text{CO}(2-1)} = -45 \pm 77 \mu\text{K}^2 h^{-3} \text{Mpc}^3$, while our visibility-domain analysis of the same data finds $P(k)_{\text{CO}(2-1)} = 190 \pm 60 \mu\text{K}^2 h^{-3} \text{Mpc}^3$ if all power is ascribed to CO(2–1), without correction for sample variance effects. In this appendix we examine the image-domain power spectrum analysis of that paper using the simulation tools developed for our visibility analysis procedure. We expect that a visibility-domain analysis will produce something close to a minimum-variance estimate of the power, and we have extensively evaluated our method for biases using simulations and found it to reliably measure the correct power on average. We are therefore most interested in characterizing any biases or uncertainty differences that arise through the image-domain analysis.

Our simulated data sets are based on the ASPECS LP 3 mm observations. We replace the visibility data with combinations of synthetic noise, with properties derived from the data themselves and mock galaxy distributions. The mock galaxy catalogs are based on the luminosity function fits found in Decarli et al. (2019). We assume the sources to be delta function-like in both spectral and spatial domains, so that there is no potential impact from resolving individual sources. The position of each galaxy was randomized for during each trial, with no attempt to mimic clustering or large-scale structure, over a volume approximately 10 times larger than the mosaicked area covered by ASPECS. To

simplify interpretation, we adjust the luminosity of all objects in a single mock catalog so that the mean power measured from the full volume is equal to $P(k) = 200 \mu\text{K}^2 h^{-3} \text{Mpc}^3$ when normalized to the redshift for CO(2–1) ($z \approx 1.3$).

Once we have synthetic data containing realistic noise and galaxy distributions, we follow the methodology laid out in Uzgil et al. (2019). Data are spectrally averaged down by a factor of 40, such that the channel resolution becomes 156.25 MHz. Visibilities for each pointing of the mosaic are split into one of four subsets of data. Data from each subset are then independently imaged using natural weighting and are mosaicked together, with a correction for the attenuation of the primary beam applied to the mosaicked map. A $110'' \times 110''$ region from the mosaicked dirty map is extracted, which roughly fits within the half-power point of the mosaicked area. Though we have not added continuum sources, we do replicate the filtering process designed to remove them, subtracting of a linear fit across frequency to the emission at given position in the sky. The resultant image cubes are then converted to brightness temperature units (in kelvin, from the more typical jansky per beam found in interferometric images), Fourier transformed, and cross-correlated against one another, with the results of the autocorrelations dropped in order to prevent noise from positively biasing the measurement. Data are converted to power spectrum units of $\mu\text{K}^2 h^{-3} \text{Mpc}^3$, utilizing the projection appropriate for CO(2–1), after which the data are binned into a 1D power spectrum. Data from the $\eta = 0$ plane are not included, as the continuum fitting procedure above will have removed all power from that set of modes. Similarly, data from the column of modes where the uv -distance is zero are also removed, as an interferometer should not contain information on the set of “zero-spacing” modes.

The distribution of power spectra measured in 100 trials of these simulations is shown in Figure B1. The gray area represents the 16%–84% range, and a similar width is found in noise-only simulations, indicating that the measurement noise dominates over variance in the galaxy catalog. There are significant deviations from the injected power at several wavenumbers, particularly for $k \lesssim 10 h \text{Mpc}^{-1}$, which roughly corresponds to the shortest baselines present within the data set. There is also strong attenuation for $k \gtrsim 50 h \text{Mpc}^{-1}$, exceeding 50% for $k \gtrsim 80 h \text{Mpc}^{-1}$. Uzgil et al. (2019) hypothesized that the attenuation is the result of resolving the map on size scales

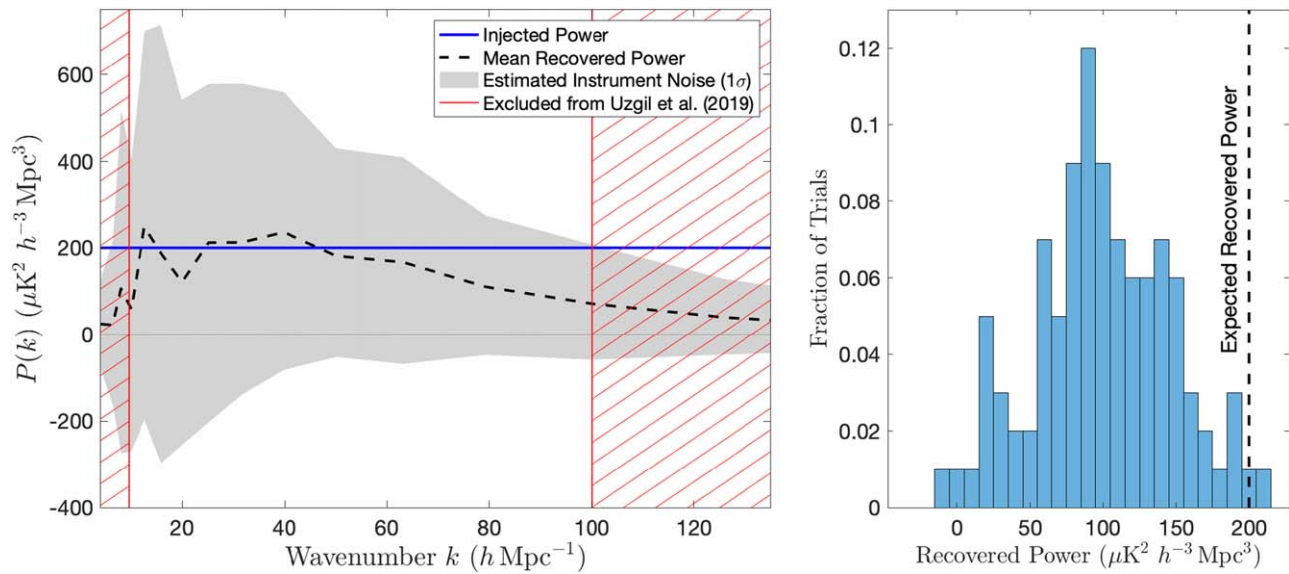


Figure B1. Left: the power spectrum recovered using the methodology from Uzgil et al. (2019). The mean injected power is shown with a blue horizontal line, the mean recovered power with a black dashed line. The gray region represents the 16%–84% range for the 100 independent mock observations. The power spectrum is analyzed with bins of width $4.1 \, h \, \text{Mpc}^{-1}$, in order to match the bin widths used in Uzgil et al. (2019). The areas excluded by the analysis of Uzgil et al. (2019) are indicated in red. Right: a histogram of band-averaged measurements for each trial, using inverse-variance weighting with incorrectly estimated per-bin variances. For the data shown here, we have also accounted for the $\approx 15\%$ loss due to channel resolution effects. The mean recovered power across all trials is approximately a factor of 2 below the true power in the simulations.

of the synthesized beam, although at $\approx 2''$ resolution, one would expect to see such effects at $\approx 130 \, h \, \text{Mpc}^{-1}$, as seen in Figure 4. In further testing with different array configurations for the ALMA 12 m array, simulating a range of hour angle coverages, we find that the recovered power for this image-space analysis is highly sensitive to the uv coverage, with less uniform coverage giving rise to more anomalous structure in the recovered power spectrum. This suggests that the source of the apparent structure is the nonuniform nature of the synthesized aperture of the interferometer. While uniform weighting of the data may help to mitigate this (e.g., Mertens et al. 2020), the use of natural weighting may actually exacerbate such issues, particularly in the case where the noise performance of different elements of the interferometer varies.

In attempting to derive the most sensitive measurement possible, Uzgil et al. (2019) used inverse-variance weighting to combine the individual bins of the power spectrum to provide a single band-averaged value (as was done in Section 3.2 here). Their weighting relies on bin uncertainties derived from the correlation products of jackknifed maps, whose power spectrum noise statistics are expected to be very similar to those shown in Figure B1 (left). Unfortunately, the attenuation of high- k modes affects both signal *and* noise, which leads to an underestimation of the variance in the high- k bins and thus their overweighting in the overall average. In Figure B1 (right), we show the recovered average power when we replicate this procedure, using the variances derived for each bin from the 100 trials, represented as the gray areas in the left panel. The recovered power is $120 \, \mu\text{K}^2 \, h^{-3} \, \text{Mpc}^3$ averaging over $9.55 \leq k \leq 100.05 \, h \, \text{Mpc}^{-1}$ (matching the Uzgil et al. (2019) range), and $80 \, \mu\text{K}^2 \, h^{-3} \, \text{Mpc}^3$ averaging over the full $4.11 \leq k \leq 130.9 \, h \, \text{Mpc}^{-1}$ range of the data. Uzgil et al. (2019) do publish a separate result for the range $9.55 \leq k \leq 55.0 \, h \, \text{Mpc}^{-1}$, which we note is relatively free of the aforementioned effects. We use the value they measure over this interval, $P(k) = -260 \pm 170 \, \mu\text{K}^2 \, h^{-3} \, \text{Mpc}^3$, in our discussion of different experiments in Section 5.4.

The mock catalogs used to test this method use galaxies with zero line width. However, the previous appendix notes the potential for signal loss due to the interplay of the galaxy emission lines and the spectral resolution of the data. The image-domain analysis of Uzgil et al. (2019) average over 40 channels, corresponding to a channel resolution of $\Delta v_{\text{chan}} \simeq 450 \, \text{km s}^{-1}$, comparable to the line widths of the source population under study. As discussed in Appendix A, this results in losses from channel resolution effects to be maximized, which should introduce an additional 15% loss. After accounting for this effect, we estimate that the recovered power in simulations that contain $200 \, \mu\text{K}^2 \, h^{-3} \, \text{Mpc}^3$ will be $100 \, \mu\text{K}^2 \, h^{-3} \, \text{Mpc}^3$ averaging over $9.55 \leq k \leq 100.05 \, h \, \text{Mpc}^{-1}$, and $70 \, \mu\text{K}^2 \, h^{-3} \, \text{Mpc}^3$ averaging over $4.11 \leq k \leq 130.9 \, h \, \text{Mpc}^{-1}$.

We note that while deconvolution might appear to help resolve the issue raised here by effectively filling in the missing information in the uv -domain, it is likely to give rise to problems akin to “mode-mixing” (Datta et al. 2010; Morales et al. 2012), where power may effectively cast throughout the (u, v, η) domain, potentially destroying the spatial scale information one hopes to recover in a power spectrum measurement. As such, methods like CLEAN (Högbom 1974) are unlikely to prove useful with image domain-based intensity mapping analyses.

ORCID iDs

Garrett K. Keating <https://orcid.org/0000-0002-3490-146X>
 Daniel P. Marrone <https://orcid.org/0000-0002-2367-1080>
 Geoffrey C. Bower <https://orcid.org/0000-0003-4056-9982>
 Ryan P. Keenan <https://orcid.org/0000-0003-1859-9640>

References

- Beckwith, S. V. W., Stiavelli, M., Koekemoer, A. M., et al. 2006, *AJ*, **132**, 1729
- Behroozi, P. S., Wechsler, R. H., & Conroy, C. 2013, *ApJ*, **770**, 57
- Bernal, J. L., Breyse, P. C., & Kovetz, E. D. 2019, *PhRvL*, **123**, 251301

- Bock, D. C. J., Bolatto, A. D., Hawkins, D. W., et al. 2006, *Proc. SPIE*, **6267**, 626713
- Bolatto, A. D., Wolfire, M., & Leroy, A. K. 2013, *ARA&A*, **51**, 207
- Bonato, M., Liuzzo, E., Giannetti, A., et al. 2018, *MNRAS*, **478**, 1512
- Bond, J. R., Jaffe, A. H., & Knox, L. 1998, *PhRvD*, **57**, 2117
- Bower, G., Keating, G., Marrone, D., et al. 2015, *IAUGA*, **29**, 2250511
- Breysse, P. C., Kovetz, E. D., & Kamionkowski, M. 2014, *MNRAS*, **443**, 3506
- Carilli, C. L., & Walter, F. 2013, *ARA&A*, **51**, 105
- Cheng, Y.-T., Chang, T.-C., Bock, J., Bradford, C. M., & Cooray, A. 2016, *ApJ*, **832**, 165
- Cleary, K., Bigot-Sazy, M.-A., Chung, D., et al. 2016, AAS Meeting, **227**, 426.06
- Crites, A. T., Bock, J. J., Bradford, C. M., et al. 2014, *Proc. SPIE*, **9153**, 91531W
- Daddi, E., Dannerbauer, H., Liu, D., et al. 2015, *A&A*, **577**, A46
- Dame, T. M., Hartmann, D., & Thaddeus, P. 2001, *ApJ*, **547**, 792
- Dannerbauer, H., Daddi, E., Riechers, D. A., et al. 2009, *ApJL*, **698**, L178
- Datta, A., Bowman, J. D., & Carilli, C. L. 2010, *ApJ*, **724**, 526
- Decarli, R., Walter, F., Aravena, M., et al. 2016, *ApJ*, **833**, 69
- Decarli, R., Walter, F., González-López, J., et al. 2019, *ApJ*, **882**, 138
- Delabrouille, J., Abitbol, M. H., Aghanim, N., et al. 2019, arXiv:1909.01591
- Downes, D., & Solomon, P. M. 1998, *ApJ*, **507**, 615
- Dwek, E., Staguhn, J. G., Arendt, R. G., et al. 2011, *ApJ*, **738**, 36
- Fonseca, J., Silva, M. B., Santos, M. G., & Cooray, A. 2017, *MNRAS*, **464**, 1948
- Frerking, M. A., Langer, W. D., & Wilson, R. W. 1982, *ApJ*, **262**, 590
- Gong, Y., Cooray, A., Silva, M. B., Santos, M. G., & Lubin, P. 2011, *ApJL*, **728**, L46
- González-López, J., Decarli, R., Pavesi, R., et al. 2019, *ApJ*, **882**, 139
- Guilloteau, S., Delannoy, J., Downes, D., et al. 1992, *A&A*, **262**, 624
- Heeschen, D. S. 1975, *S&T*, **49**, 344
- Ho, P. T. P., Moran, J. M., & Lo, K. Y. 2004, *ApJL*, **616**, L1
- Högbom, J. A. 1974, *A&AS*, **15**, 417
- Iguchi, S., Morita, K.-I., Sugimoto, M., et al. 2009, *PASJ*, **61**, 1
- Jaeger, S. 2008, in ASP Conf. Ser. 394, *Astronomical Data Analysis Software and Systems XVII*, ed. R. W. Argyle, P. S. Bunclark, & J. R. Lewis (San Francisco, CA: ASP), 623
- Kaiser, N. 1982, *MNRAS*, **198**, 1033
- Kamenetzky, J., Rangwala, N., Glenn, J., Maloney, P. R., & Conley, A. 2016, *ApJ*, **829**, 93
- Karkare, K. S., & Bird, S. 2018, *PhRvD*, **98**, 043529
- Keating, G. K., Bower, G. C., Marrone, D. P., et al. 2015, *ApJ*, **814**, 140
- Keating, G. K., Marrone, D. P., Bower, G. C., et al. 2016, *ApJ*, **830**, 34
- Keenan, R. P., Marrone, D. P., & Keating, G. K. 2020, *ApJ*, submitted
- Kennicutt, R. C., Jr. 1998, *ApJ*, **498**, 541
- Keres, D., Yun, M. S., & Young, J. S. 2003, *ApJ*, **582**, 659
- Kovetz, E. D., Viero, M. P., Lidz, A., et al. 2017, arXiv:1709.09066
- Lagache, G. 2018, in IAU Symp. 333, *Peering toward Cosmic Dawn*, ed. V. Jelić & T. van der Hulst (Cambridge: Cambridge Univ. Press), 228
- Lagos, C. D. P., Baugh, C. M., Lacey, C. G., et al. 2011, *MNRAS*, **418**, 1649
- Lagos, C. d. P., Crain, R. A., Schaye, J., et al. 2015, *MNRAS*, **452**, 3815
- Lenkić, L., Bolatto, A. D., Förster Schreiber, N. M., et al. 2020, *AJ*, **159**, 190
- Lewis, A., Challinor, A., & Lasenby, A. 2000, *ApJ*, **538**, 473
- Li, T. Y., Wechsler, R. H., Devaraj, K., & Church, S. E. 2016, *ApJ*, **817**, 169
- Lidz, A., Furlanetto, S. R., Oh, S. P., et al. 2011, *ApJ*, **741**, 70
- Madau, P., & Dickinson, M. 2014, *ARA&A*, **52**, 415
- Mashian, N., Sternberg, A., & Loeb, A. 2015, *JCAP*, **11**, 028
- Mertens, F. G., Mevius, M., Koopmans, L. V. E., et al. 2020, *MNRAS*, **493**, 1662
- Meyer, S. S., Cheng, E. S., & Page, L. A. 1991, *ApJL*, **371**, L7
- Moradinezhad Dizgah, A., & Keating, G. K. 2019, *ApJ*, **872**, 126
- Moradinezhad Dizgah, A., Keating, G. K., & Fialkov, A. 2019, *ApJL*, **870**, L4
- Morales, M. F., Hazelton, B., Sullivan, I., & Beardsley, A. 2012, *ApJ*, **752**, 137
- Morales, M. F., & Hewitt, J. 2004, *ApJ*, **615**, 7
- Murphy, E. J., Carilli, C. L. & ngVLA Science Working Groups 2017, AAS Meeting, **229**, 348.08
- Murray, S. G., Power, C., & Robotham, A. S. G. 2013, *A&C*, **3**, 23
- Nelson, D., Springel, V., Pillepich, A., et al. 2019, *ComAC*, **6**, 2
- Obreschkow, D., Croton, D., De Lucia, G., Khochfar, S., & Rawlings, S. 2009, *ApJ*, **698**, 1467
- Obreschkow, D., & Rawlings, S. 2009, *ApJL*, **696**, L129
- Padmanabhan, H. 2018, *MNRAS*, **475**, 1477
- Parsons, A., Pober, J., McQuinn, M., Jacobs, D., & Aguirre, J. 2012, *ApJ*, **753**, 81
- Pavesi, R., Sharon, C. E., Riechers, D. A., et al. 2018, *ApJ*, **864**, 49
- Planck Collaboration, Aghanim, N., Arnaud, M., et al. 2015, arXiv:1507.02704
- Popping, G., Behroozi, P. S., & Peeples, M. S. 2015, *MNRAS*, **449**, 477
- Popping, G., Pillepich, A., Somerville, R. S., et al. 2019, *ApJ*, **882**, 137
- Popping, G., Somerville, R. S., & Galametz, M. 2017, *MNRAS*, **471**, 3152
- Popping, G., Somerville, R. S., & Trager, S. C. 2014, *MNRAS*, **442**, 2398
- Pullen, A. R., Chang, T.-C., Doré, O., & Lidz, A. 2013, *ApJ*, **768**, 15
- Pullen, A. R., Serra, P., Chang, T.-C., Doré, O., & Ho, S. 2018, *MNRAS*, **478**, 1911
- Reichardt, C. L., Shaw, L., Zahn, O., et al. 2012, *ApJ*, **755**, 70
- Riechers, D. A., Hodge, J. A., Pavesi, R., et al. 2020, *ApJ*, **895**, 81
- Riechers, D. A., Pavesi, R., Sharon, C. E., et al. 2019, *ApJ*, **872**, 7
- Righi, M., Hernández-Monteagudo, C., & Sunyaev, R. A. 2008, *A&A*, **489**, 489
- Sargent, M. T., Daddi, E., Béthermin, M., et al. 2014, *ApJ*, **793**, 19
- Schmidt, M. 1959, *ApJ*, **129**, 243
- Scott, K. S., Austermann, J. E., Perera, T. A., et al. 2008, *MNRAS*, **385**, 2225
- Scoville, N., Aussel, H., Brusa, M., et al. 2007, *ApJS*, **172**, 1
- Sharp, M. K., Marrone, D. P., Carlstrom, J. E., et al. 2010, *ApJ*, **713**, 82
- Shinnaga, H., Humphreys, E., Indebetouw, R., et al. 2015, in ASP Conf. Ser. 499, *Revolution in Astronomy with ALMA: The Third Year*, ed. D. Iono et al. (San Francisco, CA: ASP), 355
- Silva, M., Santos, M. G., Cooray, A., & Gong, Y. 2015, *ApJ*, **806**, 209
- Smoot, G. F., Bennett, C. L., Kogut, A., et al. 1992, *ApJL*, **396**, L1
- Strukov, I. A., Brukhanov, A. A., Skulachev, D. P., & Sazhin, M. V. 1992, *SvAL*, **18**, 153
- Sun, G., Hensley, B. S., Chang, T.-C., Doré, O., & Serra, P. 2019, *ApJ*, **887**, 142
- Switzer, E. R. 2017, *ApJ*, **838**, 82
- Tacconi, L. J., Genzel, R., & Sternberg, A. 2020, arXiv:2003.06245
- Tacconi, L. J., Neri, R., Genzel, R., et al. 2013, *ApJ*, **768**, 74
- Tinker, J., Kravtsov, A. V., Klypin, A., et al. 2008, *ApJ*, **688**, 709
- Tinker, J. L., Robertson, B. E., Kravtsov, A. V., et al. 2010, *ApJ*, **724**, 878
- Uzgil, B. D., Aguirre, J. E., Bradford, C. M., & Lidz, A. 2014, *ApJ*, **793**, 116
- Uzgil, B. D., Carilli, C., Lidz, A., et al. 2019, *ApJ*, **887**, 37
- Visbal, E., & Loeb, A. 2010, *JCAP*, **11**, 16
- Visbal, E., Trac, H., & Loeb, A. 2011, *JCAP*, **8**, 10
- Walter, F., Decarli, R., Sargent, M., et al. 2014, *ApJ*, **782**, 79
- Watkins, L. L., van der Marel, R. P., Sohn, S. T., & Evans, N. W. 2019, *ApJ*, **873**, 118
- White, M., Carlstrom, J. E., Dragovan, M., & Holzappel, W. L. 1999, *ApJ*, **514**, 12
- Wootten, A. 2003, *Proc. SPIE*, **4837**, 110
- Yang, S., Pullen, A. R., & Switzer, E. R. 2019, *MNRAS*, **489**, L53
- Yue, B., & Ferrara, A. 2019, *MNRAS*, **490**, 1928
- Zavala, J. A., Casey, C. M., da Cunha, E., et al. 2018, *ApJ*, **869**, 71